
UNIVERSIDADE ESTADUAL DE CAMPINAS
IFGW - Instituto de Física Gleb Wataghin

Bruno Passarelli Gelli

# Caracterização de *Wavelength Shifters* e otimização do dispositivo *ARAPUCA*

# Characterization of Wavelength Shifters and Optimization of the *ARAPUCA* device

Campinas
2019

Bruno Passarelli Gelli

# Characterization of Wavelength Shifters and Optimization of the *ARAPUCA* device

# Caracterização de *Wavelength Shifters* e otimização do dispositivo *ARAPUCA*

Dissertation presented to the "Gleb Wataghin" Institute of Physics of the University of Campinas in partial fulfillment of the requirements for the degree of Master physics, in the area of Applied Physics.

Dissertação apresentada ao Instituto de Física "Gleb Wataghin" da Universidade Estadual de Campinas como parte dos requisito exigidos para a obtenção do titulo de Mestre em Física, na área de Física Aplicada.

Supervisor/Orientador: Prof. Dr. Ettore SEGRETO

Este trabalho corresponde a Versão final da dissertação defendida pelo aluno Bruno Passarelli Gelli, e orientada pelo Prof. Dr. Ettore Segreto

Campinas
2019

Ficha catalográfica
Universidade Estadual de Campinas
Biblioteca do Instituto de Física Gleb Wataghin
Lucimeire de Oliveira Silva da Rocha - CRB 8/9174

G282c

Gelli, Bruno Passarelli, 1995-
Characterization of wavelength shifters and optimization of the ARAPUCA device / Bruno Passarelli Gelli. – Campinas, SP : [s.n.], 2019.

Orientador: Ettore Segreto.
Dissertação (mestrado) – Universidade Estadual de Campinas, Instituto de Física Gleb Wataghin.

1. Experimento DUNE. 2. Detectores de neutrinos. 3. Argônio líquido. 4. Deslocador de comprimento de onda. I. Segreto, Ettore, 1973-. II. Universidade Estadual de Campinas. Instituto de Física Gleb Wataghin. III. Título.

Informações para Biblioteca Digital

**Título em outro idioma:** Caracterização de wavelength shifters e otimização do dispositivo ARAPUCA
**Palavras-chave em inglês:**
DUNE experiment
Neutrino detectors
Liquid argon
Wavelength shifters
**Área de concentração:** Física Aplicada
**Titulação:** Mestre em Física
**Banca examinadora:**
Ettore Segreto [Orientador]
Douglas Galante
Francisco das Chagas Marques
**Data de defesa:** 20-06-2019
**Programa de Pós-Graduação:** Física

**Identificação e informações acadêmicas do(a) aluno(a)**
- ORCID do autor: https://orcid.org/0000-0002-9354-9371
- Currículo Lattes do autor: http://lattes.cnpq.br/7001798328688694

MEMBROS DA COMISSÃO JULGADORA DA DISSERTAÇÃO DE MESTRADO DE **BRUNO PASSARELLI GELLI – RA 150897** APRESENTADA E APROVADA AO INSTITUTO DE FÍSICA "GLEB WATAGHIN", DA UNIVERSIDADE ESTADUAL DE CAMPINAS, EM 28 / 06 / 2019.

**COMISSÃO JULGADORA:**

**- Prof. Dr. Ettore Segretto – Orientador – DRCC/IFGW/UNICAMP**
**- Prof. Dr. Douglas Galante – CNPEM**
**- Prof. Dr. Francisco das Chagas Marques – DFA/IFGW/UNICAMP**

**OBS**.: Ata da defesa com as respectivas assinaturas dos membros encontra-se no SIGA/Sistema de Fluxo de Dissertação/Tese e na Secretaria do Programa da Unidade.

CAMPINAS
2019

# Agradecimento

Nessa seção eu gostaria de agradecer a todos que me auxiliaram durante este trabalho.

Primeiramente, eu gostaria de agradecer aos meus pais e minha família. Sem vocês e todo seu apoio nada seria possível!

Gostaria de agradecer também à Maria Clara por todo seu apoio e todas as discussões que tivemos. Ambos foram fundamentais e essenciais para este trabalho!

Ao Prof. Dr. Ettore Segreto, que mais do que apenas um orientador, foi um amigo, meu sincero obrigado. Seu dedicação e seus ensinamentos foram essenciais para este trabalho. Agradeço também à Profa. Dra. Ana Amélia Machado, a qual considero minha coorientadora, seu auxilio foi fundamental para o desenvolvimento deste trabalho, bem como todas as discussões e conselhos.

Devo também uma menção aos meu amigos e colegas, que sempre estiveram lá para me ajudar, aconselhar e descontrair. Obrigado por tudo. Destaco aqui meus amigos e para sempre colegas de laboratório Cecília, Glauber, Greg, Henrique, Heriques, Jully, Rafaela, Renan, Renato e Marina. Obrigado pelas discussões, conversas e noites mal dormidas trabalhando juntos!

Agradeço também a todos os professores que eu tive, cujos ensinamentos me proporcionaram a capacidade de desenvolver este trabalho. Em especial, agradeço ao professores Prof. Dr. Marcelo Guzzo, Prof. Dr Rickson Mesquita e Prof. Marcelo Mason. Que sempre estiveram dispostos a conversar e me aconselhar, mesmo nas horas mais difíceis.

Aos tecnícos de funcionários do IFGW, em especial ao Cesar, Costa, Fábio e Vladmir, meu sincero obrigado. Por sempre estarem dispostos a me ajudar, mesmo com os pedidos mais inusitados e prazos curtos.

Por fim, agradeço à equipe da linha TGM no LNLS. Em especial ao Prof. Dr. Douglas Galante e à Dr. Verônica Teixeira, cujo o auxilio foi essencial para a realização e análise das medidas feitas no LNLS.

O presente trabalho foi realizado com apoio da *Coordenação de Aperfeiçoamento de Pessoal de Nível Superior* - Brasil (CAPES) - Código de Financiamento 001

# Resumo

A próxima geração de experimentos de neutrinos oferece grandes desafios na tecnologia de coleção de luz de cintilação. O detector Arapuca, desenvolvido por nosso grupo, se situa como um candidato promissor no cenário de novos detectores de luz para estes experimentos. Seu funcionamento se baseia em uma combinação inteligente de Wavelength Shifters. Neste trabalho estudamos estes componentes, caracterizando suas propriedades físicas ainda não completamente conhecidas.

O padrão temporal de emissão dos mais comuns wavelength shifters foi medido utilizando a linha de luz TGM, no LNLS, operando no modo *single bunch beam*. O resultado destas medidas exibe a existência de *delayed light emission* e seu tempo característico. Este fato corrobora à hipotese de ionização destes compostos quando expostos a fótons de alta energia, como os oriundos da cintilação do argônio líquido.

Como um aprofundamento no estudo da ionização, a eficiência relativa de conversão destes compostos foi medida. Esta análise apresenta um primeiro passo no entendimento de como o efeito de ionização destas moléculas pode contribuir na eficiência deste composto. Um resultado obtido destas medidas é a eficiência de conversão de luz de cintilação do argônio líquido para diferentes espessuras de TPB, que concorda o encontrado na literatura porém com maior precisão e mais dados.

A eficiência relativa dos compostos também foi medida utilizando luz no ultravioleta próximo, com o intuito de estudar o melhor candidato à wavelength shifter interno no dispositivo ARAPUCA. Foi encontrado que o BisMSB apresenta uma eficiência superior ao TPB quando excitado utilizando o espectro de emissão do pTP. Isto se mostrou um resultado importante, visto que o custo deste novo composto é aproximadamente três vezes menor do que o composto atual, o TPB.

Por fim, uma simulação Monte Carlo detalhada do dispositivo ARAPUCA foi desenvolvida. O intuito foi comparar sua eficiência com uma nova iteração deste dispositivo, o X-ARAPUCA nas dimensões do fotodetector padrão do DUNE.

Neste estudo foram variados diversos parâmetros, respeitando as restrições impostas pelo design. Foi encontrado que o X-ARAPUCA apresenta uma eficiência significativamente maior do que o ARAPUCA padrão. O X-ARAPUCA representa o sistema base de fotodetecção para o detector distante do DUNE.

# Abstract

The next generation of neutrino experiments offers major challenges in collection of scintillation light. The ARAPUCA device, developed by our group, stands as a promising candidate in the scenario of new light detectors for these experiments. Its operation is based on a combination of Wavelength Shifters and a Dichroic Filter. In this work, we studied this compounds, characterizing some of their physical properties.

The temporal emission pattern of the most common wavelength shifters was measured using the TGM beamline in the LNLS, operating in the *single bunch beam* mode. The result of these measurements shows the existence of *delayed light emission* and its characteristic time. This fact corroborates the hypothesis of ionization of these compounds when exposed to high energy photons, such as those from the liquid argon scintillation.

As a further study of ionization, the relative conversion efficiency of these compounds was measured. This analysis presents a first step in the understanding of how the ionization of these molecules can contribute to the efficiency of this compound. A result obtained from these measurements is the conversion efficiency of liquid argon scintillation photons for different thicknesses of TPB. The results agree with what is found in the literature, with good precision and in a wider range with respect to the previous measurement.

The relative efficiency of the compounds was also measured using visible and near ultraviolet light, in order to study the best candidate for the internal wavelength shifter in the ARAPUCA device. It has been found that BisMSB exhibits superior efficiency to TPB when excited using the emission spectrum of pTP. This is an important result, since the cost of this compound is approximately three times lower than the current compound, TPB.

Finally, a detailed Monte Carlo simulation of the ARAPUCA device was developed. The intention was to compare its efficiency with a new iteration of this device, the X-ARAPUCA. In this study, several parameters were varied, respecting the restrictions imposed by the DUNE standard photodetector design. It has

been found that X-ARAPUCA has an efficiency significantly higher than a standard ARAPUCA. The X-ARAPUCA represents the baseline design of the photodetection system of the DUNE far detector.

# List of Figures

# List of Abbreviations

| | |
|---|---|
| **ADC** | **A**nalog to **D**igital **C**onverter |
| **DUNE** | **D**eep **U**nderground **N**eutrino **D**etector |
| **FD** | **F**ar **D**etector |
| **IRF** | **I**mpulse to **R**esponse **F**unction |
| **LAr** | **L**iquid **Ar**gon |
| **LArTPB** | **L**iquid **Ar**gone **T**ime **P**rojection **C**hamber |
| **LET** | **L**inear **E**nergy **T**rasnfer |
| **LNLS** | Brazilian Synchrotron Light Laboratory |
| **ND** | **N**ear **D**etector |
| **PE** | **P**hoto**E**mission |
| **PL** | **P**hoto**L**uminescence |
| **PMT** | **P**hoto**m**ultiplier **T**ube |
| **PSD** | **P**ulse **S**hape **D**iscrimination |
| **QE** | **Q**uantum **E**fficiency |
| **SiPM** | **Si**licon **P**hoto**M**ultiplier |
| **SURF** | **S**anfordr **U**nderground **R**esearch **L**aboratory |
| **TGM** | **T**oroidal **G**rating **M**onochromator |
| **TUM** | **T**echnische **U**niversität **M**ünchen |
| **UNICAMP** | **Uni**versity of **Camp**inas |
| **UV** | **U**ltra **V**iolet |
| **UV-Vis** | **U**ltra **V**iolet to **Vis**ible |
| **VUV** | **V**acuum **U**ltra **V**iolet |
| **WLS** | **W**ave **L**ength **S**hifter |
| **BisMSB** | 1,4-**Bis**(2-**M**ethyl**S**tyryl)**B**enzene |
| **POPOP** | 1,4-Bis(5-phenyl-2-oxazolyl)benzene |
| **PPO** | 2,5-Diphenyloxazole |
| **PTFE** | **P**oly**t**etra**f**luoro**e**thylene |
| **pTP** | **p**-**T**er**P**henyl |
| **TPB** | 1,1,4,4-**T**etra**P**henyl-1,3-**B**utadiene |

# List of Symbols

| | | |
|---|---|---|
| $W_1$ | Ionization Potential | $eV$ |
| $\tau_f$ | Fast decay component | $ns$ |
| $\tau_s$ | Fast decay component | $ns$ |
| $\tau_i$ | Intermediary decay component | $ns$ |
| $\lambda$ | Wavelength | $nm$ |
| $I_0$ | Beam intensity | $mA$ |
| $I^m$ | Measured intensity | $mA$ |
| $I_{sample}$ | Sample response intensity | $mA$ |
| $B$ | Background intensity | $mA$ |
| $F$ | Filter Transmitance | |
| $f_{solidangle}$ | Detector solid angle | |
| $P$ | PMT's QE correction | |
| $\alpha$ | Alpha | |
| $e^-$ | Electron | |
| $\nu_e$ | Electron Neutrino | |
| $\mu^-$ | Muon | |
| $\nu_\mu$ | Muon Neutrino | |
| $\gamma$ | Photon | |
| $\tau^-$ | Tau | |
| $\nu_\tau$ | Tau Neutrino | |
| $Ar_2^*$ | Excited Argon Molecule | |
| $Ar_2^+$ | Ionized Argon Molecule | |
| $Ar_2^{**}$ | Double excited Argon Molecule | |
| ${}^1\Sigma_g^+$ | Ground State | |
| ${}^1\Sigma_e^+$ | Singlet State | |
| ${}^3\Sigma_e^+$ | Triplet State | |
| $S_n$ | Excited singlet state | |
| $S_1$ | Lowest excited singlet state | |

| | |
|---|---|
| $T_n$ | Excited triplet state |
| $T_1$ | Lowest excited triplet state |

# Contents

# Chapter 1

# DUNE

Neutrinos are elementary particles, belonging to the lepton family. Its name comes from the fact that this particles are electrically neutral and have a small mass ($< 2\ eV$). [1] This present a challenge to the detection of this particles, since it is only allowed to interact through weak force, and its interaction cross-section is small. Neutrinos exist in three flavors, Electron Neutrino ($\nu_e$), Muon Neutrino ($\nu_\mu$) and Tau Neutrino ($\nu_\tau$). These are associated with their respective charged leptons, the electron ($e^-$), Muon ($\mu^-$) and Tau ($\tau^-$). [2]

To properly study many neutrinos' characteristics, a highly specialized detector has to be used. The DUNE (*Deep Underground Neutrino Experiment*) will be one of the world's leading edge neutrino and proton decay observatory, being capable of studding not only many properties of neutrinos but also nucleon decay models, supernova physics and dark matter. [3] This scientific objectives at DUNE are divided in two categories, the *primary objectives* and the *auxiliary objectives*. The primary objectives, listed bellow, consist in the high priority scientific goals, focusing in fundamental questions in neutrino physics and astrophysics.

- To measure the oscillation parameters in the $\nu_\mu \longrightarrow \nu_e$ and $\bar{\nu}_\mu \longrightarrow \bar{\nu}_e$ process with great precision. This allows several open questions in the neutrino physics to be understood, as

  - the existence of CP violation in the leptonic sector;

  - The mass hierarchy of the neutrinos;
  - The actual parameters that govern the neutrino oscillation process.

- To look for proton decay events. This will be done in a lifetime range predicted in many decay models, which provides a direct probe into many GUT (*Grand Unification Theories*) models. [4]

- To measure the electron neutrinos flux from a *Core-Collapse Supernova* inside the Milky Way.

Due to DUNE's massive size, advanced technology and the powerful neutrino beam, other several Auxiliary Objectives are possible to achieve. They include,

- The measurement of several Neutrino Cross-Sections;

- The search for Dark Matter candidates;

- Measurements on neutrino oscillation using atmospheric neutrinos;

- And many others. [5]

The scientific program is the core driver of the detector design, where several requirements are made so it is possible to achieve its goals. In order accomplish its objectives, the DUNE project will consists of two modern underground neutrino detectors in line with the world's most powerful neutrino beam.

The neutrino beam is in construction under the LBNF (*Long-Baseline Neutrino Facility*) project, and, once finished, it will operate at 1.2 $MW$ producing neutrinos in the 0.5 $GeV$ to 4 $GeV$ range.

The detectors are placed in two different locations, one high-precision near the beam source, and one much larger farther downstream.

The ND *(Near Detector)* will be used to fully characterize the beam's intensity and energy spectrum[1].

[1] Situated at Fermilab *(Fermi National Accelerator Laboratory)* in Batavia, Illinois.

The FD *(Far Detector)* will be placed at the SURF *(Sanford Underground Research Laboratory)* in Lead, South Dakota. This location is situated 1300$Km$ away and more than a kilometer underground[2], which will allow interesting neutrino properties to be studied, i.e. matter enhanced neutrino oscillations. This distance was carefully chosen in conjunction with the neutrino beam energy, so the effects of interest will be at its maximum. [6]

The aspects of the Far Detector will be discussed in detail in the next section.

## 1.1 DUNE Far Detector

DUNE far detector will consist of modular LArTPCs *(Liquid Argon Time Projection Chambers)* fully equipped with state of the art technology. This is a well established technology for neutrino detection that relies in the neutrinos interacting with its active medium, liquid argon. An illustration of this technology is shown in figure 1.1.

[2]This is done to block most cosmic ray and atmospheric events.

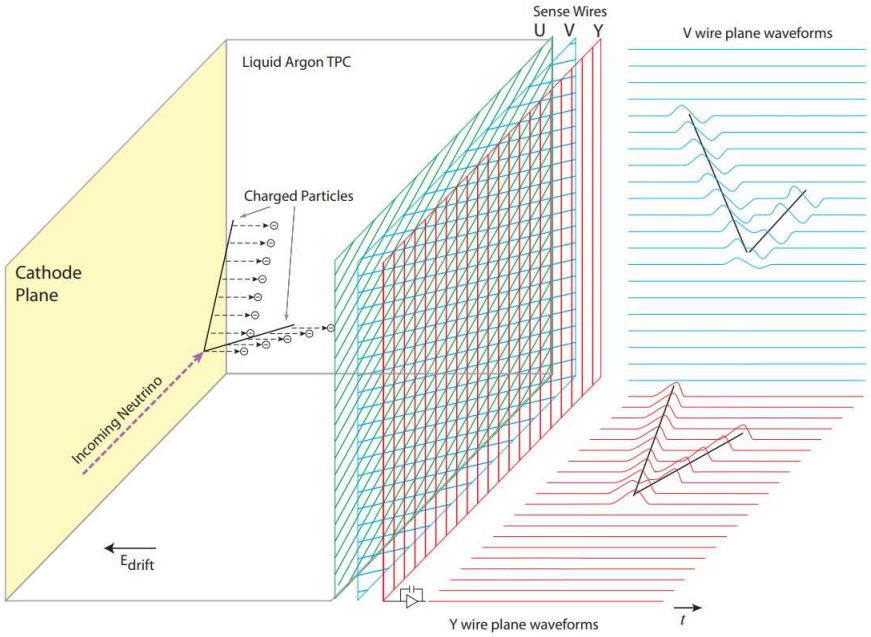


FIGURE 1.1: It is possible to observe a conceptual design of a TPC. [7] The ionized electrons shown being extracted due the high electric field ($E_{drift}$). They are directed to the anode grid, which is composed of three different planes to provide position resolution. The *U plane* (green) is shielding plane, used to smooth the electric field. The *V plane* (blue) is the induction plane, which measures the charges by the induced current they produce in the wires. The *Y plane* (red) is the collection plane, it measures the charges by collecting them.

The products of the interaction can ionize or excite the argon atoms which further produces free electrons and photons in the event location, as it was explained in details in section 2.1. By applying a strong uniform electric field it is possible to extract the free electrons and collect them in the anode, which combined with a carefully designed anode, provides 2D view of the event.

The produced photons, being much faster than the electron in the medium, can be used to retrieve the start time of the interaction. This fact can be combined with the 2D view and its own collection time, allowing a 3D reconstruction of the event topology.

It is also possible to study the calorimetry of the event using both charge and

light. This, in conjunction with the 3D event topology, allows a precise understanding of each interaction.

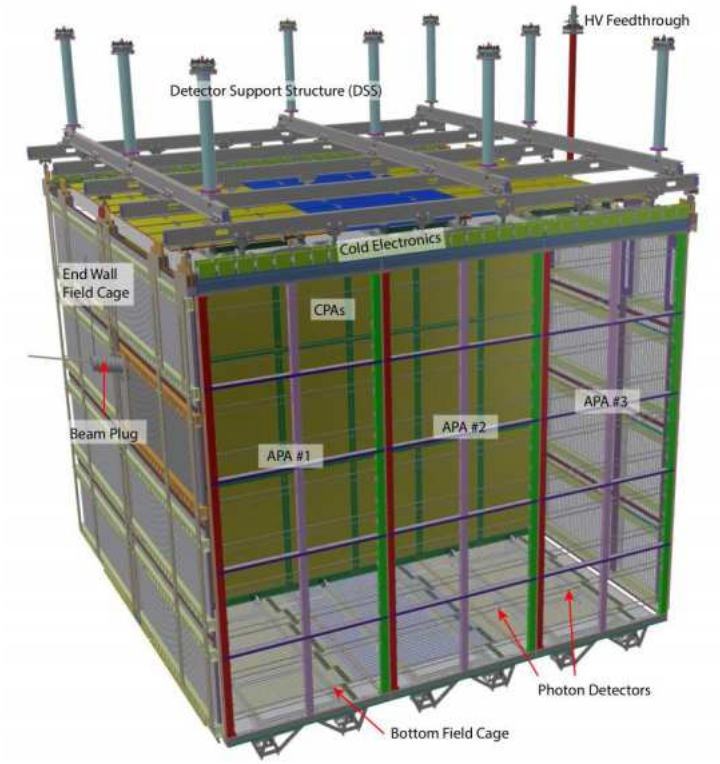


FIGURE 1.2: ProtoDUNE LArTPC design, measuring 6 $m$ × 6 $m$ × 6 $m$. The design presented is similar to the modular construction of the DUNE's LArTPC.

The requirements to achieve the expected scientific objectives demand an efficient, well instrumented and massive detector, which DUNE will address with modular LArTPCs whose combined fiducial volume sums to over 40$kton$. [3]

To achieve this impressive size, many components of the detector had to be rethought with respect to the older designs. One interesting component is the light collection system, which plays a key role in the detector. The system is located in between the field cage and the cryostat walls, where the LArTPC is not instrumented to detect particles. This fact creates a compromise between the light

collection system's size and the amount of LAr wasted outside the detector's active volume. In order to achieve the size requirements, DUNE shifts this compromise towards the least LAr wasted, putting strong constrains at light collection system's size. In figures 1.2 and 1.3 it is possible to see the tight dimensions allocated to the light collection system. [8]

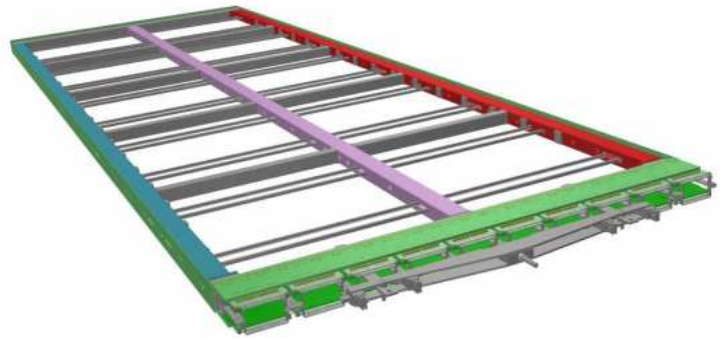

FIGURE 1.3: A detailed view form an APA *(Anode Plane Assembly)* frame, measuring 6 $m \times 2.4$ $m$. The photon detection system's modules will be placed inside the slots showed.

### 1.1.1 Light Detection in DUNE Far Detector

The new requirements on light collection system's size makes imperative the development of new technologies. Although many different designs of new technologies are being proposed, they all have to obey certain criteria in addition to the size limitations, e.g., the minimum light yield to achieve the scientific goals. Now there are 3 main candidates for photons detection system,

- Light Guide Bars; [9]
- Deep Coated Bars; [10]
- ARAPUCAs. [11]

The first two designs follows similar strategies, being primarily differentiated by the number of times LAr light will be converted. In the first design, a commercial Wavelength Shifting bar is optically coupled with TPB covered radiator plates and is instrumented in the ends with SiPMs *(Silicon Photomultipliers)*. Liquid Argon light will first interact with the TPB coated radiator plates, which will produce blue $(430nm)$ light. Since the radiator is coupled with the bar, the converted light can efficiently penetrate it and be converted again, where it can became trapped due to total internal reflection and be guided to the instrumented edges. A schematic representation of this design can be seen in figure 1.4.

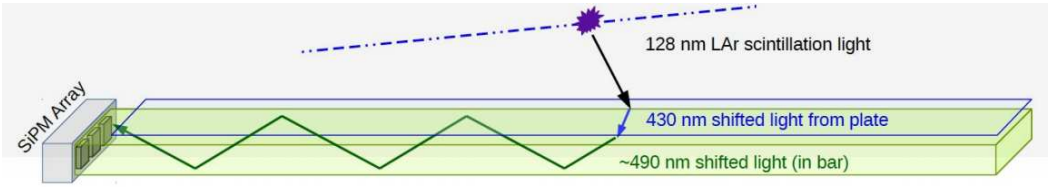


FIGURE 1.4: A schematic representation of the Light Guided Bars design. In blue is represented the Radiator Plates and in green the Wavelength Shifting polystyrene bar.

In the second design, an acrylic bar is deep-coated with TPB, creating a thin layer on the surface. LAr photons can interact with this layer, being converted it the same way described in the first design. In this case photons are not shifted for a second time, but the fraction which is trapped by total internal reflection is directly transmitted towards the SiPMs which are installed on their ends.

While both technologies display interesting solutions to the design challenges, both also present drawbacks in terms of efficiency. One particular cause is the strong angular dependency to trap photons due the use of total internal reflections.

The third design shows peculiarities and viable solutions to the drawbacks presented by the other technologies. This photodetection system will be widely discussed in section 1.2.

## 1.2 ARAPUCA

The ARAPUCA design follows a different path than the other technologies. While the other designs use total internal reflection to trap the photons inside their bars, the ARAPUCA design uses a clever combination of optical components to trap the photons. In figure 1.5, one can observe an infographic picturing the ARAPUCA's functioning mechanism.

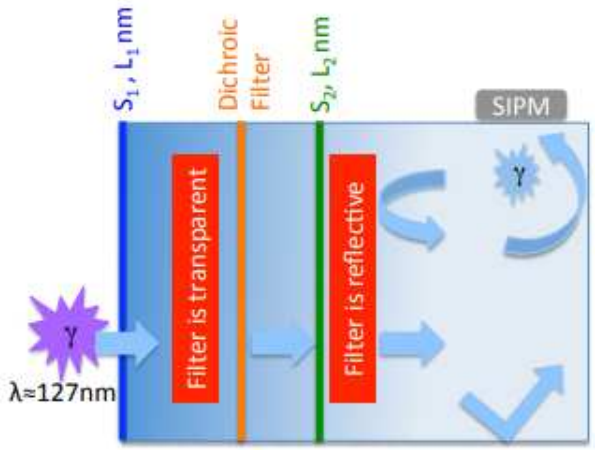


FIGURE 1.5: A schematic representation of the ARAPUCA design. $S_1$ correspond to the external WLS, $S_2$ correspond to the internal WLS.

The ARAPUCA's core component is an optical window, which is constituted by a dichroic shortpass optical filter coupled to two different wavelength shifting compounds. This optical device serves as an acceptance window for a cavity with highly reflective internal surfaces, instrumented with SiPMs.

The trapping process happens by LAr light first interacting with the external WLS, being converted to a wavelength where the dichroic filter is highly transparent. After passing through the filter, the light reaches the internal WLS, where it is converted to a wavelength where the filter is highly reflective. Once the photon undergoes the second conversion, it is trapped inside the cavity, where it will

reflect until it is detected.

In figure 1.6 it is possible to see in details the conversion cascade, responsible for the trapping effect. On the left it is shown a plot of transmitance of the dichroic filter *versus* wavelength with the first WLS's emission spectrum on top. On the right it is possible to observe a plot of reflectance of the dichroic filter *versus* wavelength with the second WLS's emission spectrum on top.

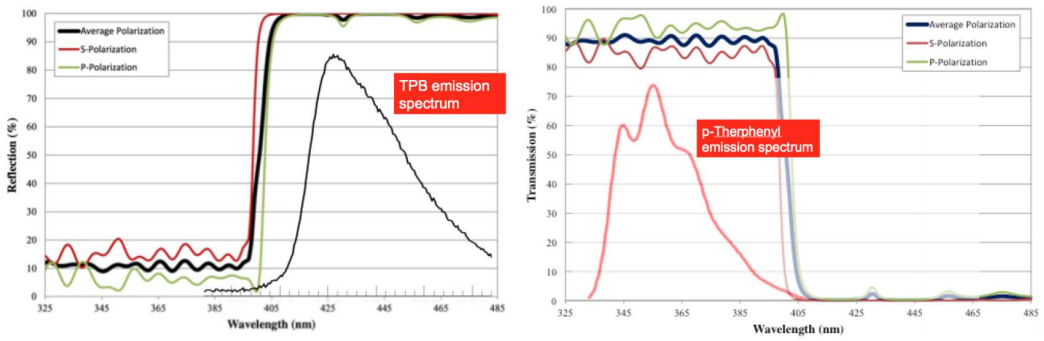


FIGURE 1.6: A plot of the dichroic filter transmitance $(\%)$ *vs* wavelength $(nm)$ with a plot of TPB emission spectrum *(left)*. A plot of the dichroic filter reflectance $(\%)$ *vs* wavelength $(nm)$ with a plot of pTP emission spectrum *(right)*.

It is easy to see that the first emission spectrum overlays nicely with the filter's transparent region, whereas the second emission spectrum overlays the filter's reflective region.

This simple but elegant designs stands out from the other two by its high efficiency. Reaching $1.15\% \pm 0.15\%$ in the latest measurements, the ARAPUCA presents an order of magnitude higher efficiency than the other designs.[12]

In this tests, as well in the explanation in this text, pTP *(p-Therphenyl)* and TPB where used as $S_1$ and $S_2$, respectively. Despite this choice, many other combinations could be used. A more detailed discussion on wavelength shifters for the ARAPUCA will be presented in section 1.2.1.

### 1.2.1 WLS for the ARAPUCA

The global detection efficiency of the device depends on the matching of the three fundamental components, which are the internal WLS $(S_1)$, the dichroic filter and the external WLS $(S_2)$. The basic ARAPUCA design uses pTP as $S_1$ and TPB as $S_2$ due to many facts, e.g.,

- both are widely used, and so are easily accessible;
- TPB shows a high efficiency in converting LAr light;
- good spectrum overlay with the $400nm$ dichroic filter properties.

Although this combination provides high efficiency, there are many commercially available WLS compounds, and the use of a better tuned combination is possible to result in a higher detection efficiency. Many other parameters regarding the wavelength shifters can also affect the total global efficiency of the device. A detailed study of the wavelength shifters properties and many parameters, regarding their use in ARAPUCA, will be discussed in chapter 3.

### 1.2.2 X-ARAPUCA

The X-ARAPUCA design is an upgrade of the ARAPUCA design. [13] It incorporates changes in the core idea that allows the device to reach even higher efficiency marks while simplifying its design. The main upgrade is the insertion of an wavelength shifting bar inside the device, which serves as $S_2$ and also as a light guide. In figure 1.7, it is possible to see an assembled and an exploded view of the design, where in white is represented the structural frame pieces. The dichroic filters are showed in light yellow and the wavelength shifting bar is depicted in light blue. The SiPM board is represented in green in the right. It is also possible to observe that in this new design there are two acceptance windows.

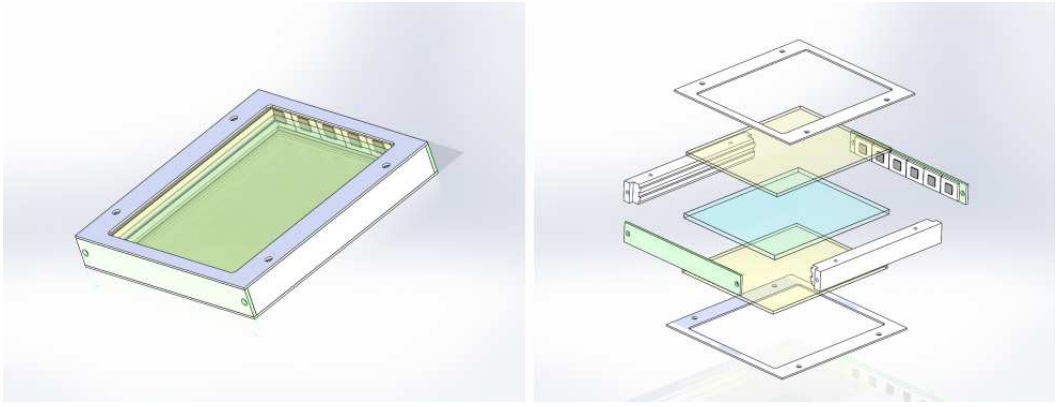

FIGURE 1.7: A schematic representation of the double faced X-ARAPUCA design. An assembled *(left)* and an exploded view *(right)*..

The basic functioning mechanism of the ARAPUCA is maintained in the new design, but different detection modes are made possible by the addition of the wavelength shifting bar. Once the converted photon enters the X-ARAPUCA, it is able to interact with the bar in the same manner as it could interact with $S_2$. If the newly converted photon forms an angle greater then the critical angle, with respect to the bar surface, it will be trapped inside the bar, where it will perform total internal reflections until it reaches the SiPMs. This mechanism, called *a-mode*, is illustrated in figure 1.8.


FIGURE 1.8: A representation of an event on X-ARAPUCA detected in the *a-mode*. In purple it is possible to observe $S_1$ plus the dichroic filter. The bar is depicted in green, and the SiPMs in black. The light blue component correspond to the reflective internal surfaces of the device.

If the angle is smaller than the critical angle, the photon can exit the bar. Since the photon undergone the second conversion, it is not allowed to escape the X-ARAPUCA through it's windows. Due this fact, the photon will reflect inside the device until it is detected at one SiPM. In figure 1.9 it is possible to observe this mode, *b-mode*. This last mode of operation is the exactly same operation mode of the ARAPUCA design.

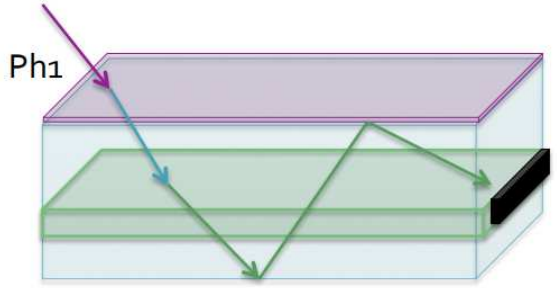


FIGURE 1.9: A representation of an event on X-ARAPUCA detected in the *b-mode*. In purple it is possible to observe $S_1$ plus the dichroic filter. The bar is depicted in green, and the SiPMs in black. The light blue component corresponds to the reflective internal surfaces of the device.

One more detection mode is possible, named *c-mode*, where a photon with high incident angle enters the gap between the filter and the bar. If the angle is high enough, this photon will undergo total internal reflection at the filter and bar surfaces until it is detected by the SiPMs. It is illustrated in figure 1.10.

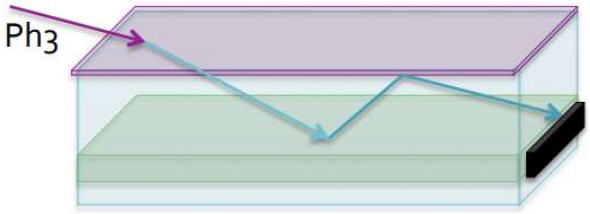


FIGURE 1.10: A representation of an event on X-ARAPUCA detected in the *c-mode*. In purple it is possible to observe $S_1$ plus the dichroic filter. The bar is depicted in green, and the SiPMs in black. The light blue component correspond to the reflective internal surfaces of the device.

This two new modes can highly increase the efficiency of the device, since the total internal reflection is 100% efficient. This addition also simplifies the device design, given the ARAPUCA requires the delicate task of covering the dichroic filter and its inside with different WLS, whereas the X-ARAPUCA only requires the dichroic filter to be coated. This addition also excludes the probability of cross contamination between $S_1$ and $S_2$, which can drastically reduce the device's efficiency.

# Chapter 2

# Liquid Argon and Wavelength Shifters

## 2.1 Liquid Argon scintillation light

One of the most important features of liquid argon, when used as scintillation medium, is its high light yield for a given energy deposition. This fact makes scintillation light an important tool in particle detection using liquid argon, as discussed in section 1. A profound knowledge of its behavior and underlying physics is mandatory for its proper use.

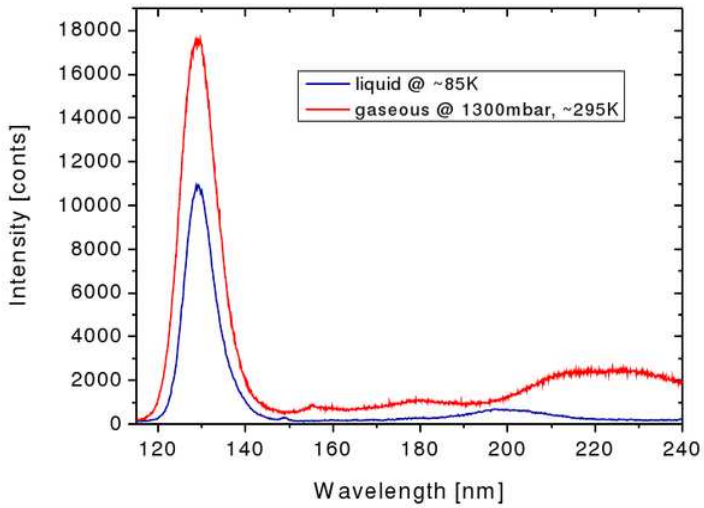


FIGURE 2.1: Emission spectrum of liquid argon (*blue*) and gaseous argon (*red*).

In the figure 2.1 it is possible to see that the emitted light has a well defined spectrum in the deep UV range. This poses a challenge for its detection, since the majority of materials is not transparent to these wavelengths. In section 2.2, these challenges will be discussed deeply and the more common solutions will be presented.

### 2.1.1 Physics of scintillation in LAr

The low ionization potential of liquid argon ($W_l \approx 23.6\,eV$) coupled with its high density are the key factors that produce the excellent scintillation light yield [14].

The passage of ionizing radiation through LAr is capable of producing electron-ion pairs (*ionization*) and argon excitons (*excitation*). The excitons quickly combine into excimers through self-trapping process, within picosecond timescale. This excimers consists in excited argon molecules ($Ar_2^*$); formally, they are Rydberg states formed by an $Ar_2^+$ core with a bound electron.

The ionization process also leads to the formation of $Ar_2^+$ through ion combination [15]. While the ejected electrons are capable of producing electron-ion pairs and excitons [16].

The excimer states decay radiatively to the ground state emitting a photon, as follows,

$$Ar_2^* \rightarrow 2Ar + \gamma \tag{2.1}$$

Produced ions recombine with electrons and then decay. Its decay chain is the following.

$$\begin{aligned} Ar_2^+ + e^- &\rightarrow Ar^{**} + Ar \\ Ar^{**} &\rightarrow Ar^* \\ Ar^* + Ar &\rightarrow Ar_2^* \\ Ar_2^* &\rightarrow 2Ar + \gamma \end{aligned} \tag{2.2}$$

As can be seen in equations 2.1 and 2.2, both excitation and ionization processes lead to the formation of argon excimer states. The excimer can have its bound electron with spin paired or unpaired, ${}^1\Sigma_u^+$ (singlet state) and ${}^3\Sigma_u^+$ (triplet state) respectively.

The ${}^1\Sigma_u^+$ decays into the ${}^1\Sigma_g^+$ (repulsive ground state), two argon atoms, emitting a photon. This process respects all selection rules and so happens quickly, with a time constant of $\tau_f \approx 6ns$.

The ${}^3\Sigma_u^+$ is forbidden to directly decay to the ground state by the selection rule $\Delta S = 0$. However, for heavy nuclei the Russel-Sunders notation is not valid and so the ${}^3\Sigma_u^+$ decays radiatively to ${}^1\Sigma_g^+$. This process occurs with a longer time scale and a time constant of $\tau_s \approx 1600ns$.

### 2.1.2 Time profile of scintillation light

Particles with different LET *(Linear Energy Transfer)* produce different amounts of ionization and excitation in LAr. This is an important aspect, since the likelihood of producing ${}^1\Sigma_u^+$ or ${}^3\Sigma_u^+$ is not equal for the two mechanisms.

The time profile of scintillation light, showed in equation 2.3, is composed of a fast $(\tau_f)$ and a slow $(\tau_s)$ exponential component, which are attributed to the ${}^1\Sigma_u^+$ and ${}^3\Sigma_u^+$ decay respectively.

$$I(t) = Ae^{-t/\tau_f} + Be^{-t/\tau_s} \tag{2.3}$$

The abundance of the two components, $A$ and $B$, are determined by the ionizing particle. In figure 2.2 it is possible to see this effect.

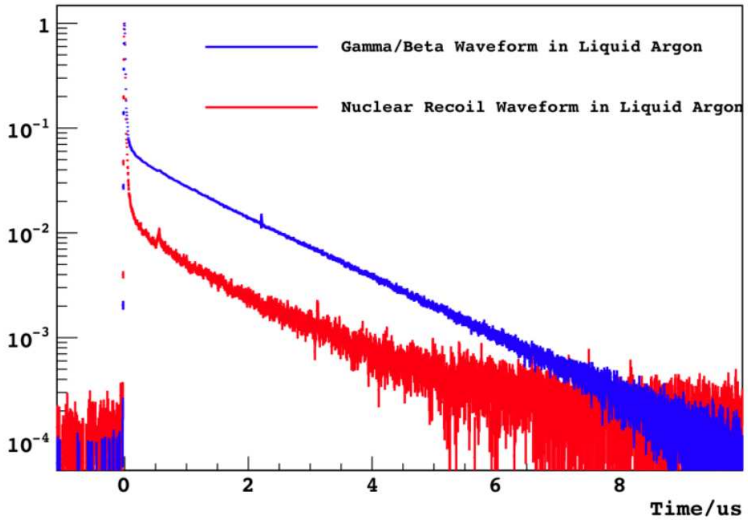


FIGURE 2.2: Average waveform obtained by irradiating LAr with $e^-/\gamma$ (*blue*) and $\alpha$ (*red*) [17].

This is the basis of the PSD (*Pulse Shape Discrimination*) technique, used in several experiments which use LAr as active medium. It heavily relies on the facts discussed in this section, and a good understanding of the physics discussed is essential for its use.

A pulse shape discrimination parameter is usually defined as follows:

$$F_{prompt} = \frac{\int_0^{t^*} I(t)dt}{\int_0^{\infty} I(t)dt}\,, \tag{2.4}$$

where $t^*$ represents the time that gives the best separation among different particles. It has been found experimentally by many groups that the optimal value for $t^*$ is around 100 $ns$ [18] [19] [20] [21].

Although PSD technique importance, some odd findings are know to happen. In the section 2.1.3, these findings will be discussed along side other unusual effects observed in liquid argon physics.

### 2.1.3 Discrepancies in Liquid Argon physics

Although the physics behind the scintillation process is well understood, some experiments show a tertiary temporal component $(\tau_i)$ with a decay time in between $\tau_f$ and $\tau_s$.

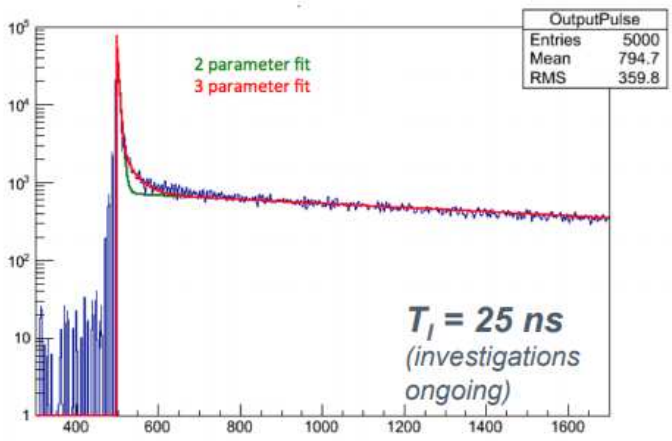


FIGURE 2.3: Average waveform in lAr with two fits on top. Green represents a two exponential fit and red a tree exponential fit. In this figure it is possible to see the existence of a third component in the LAr time profile [22].

Another unusual effect found in LAr comes from the PSD technique, where $t^*$ is found experimentally to be around $100ns$. This result is not in concordance with the $30ns$ calculated value. [23]

This discrepancy suggest that some underlying physics is not well understood, which could imply exotics mechanisms in LAr. Other explanation to this disagreement could relay in the measurement setup used in most LAr experiments. This will be discussed in depth in section 2.2.1.

## 2.2 Wavelength Shifters

The light produced in the scintillation of LAr is emitted in the VUV range and is peaked around $128nm$, as discussed in section 2.1. Light at this wavelength is difficult to detect, manly due to the lack of materials that are transparent to it and can resist cryogenic temperatures. In figure 2.4 it is possible to observe the scintillation spectra of several noble elements, along the transmitance of the most common optical window material.

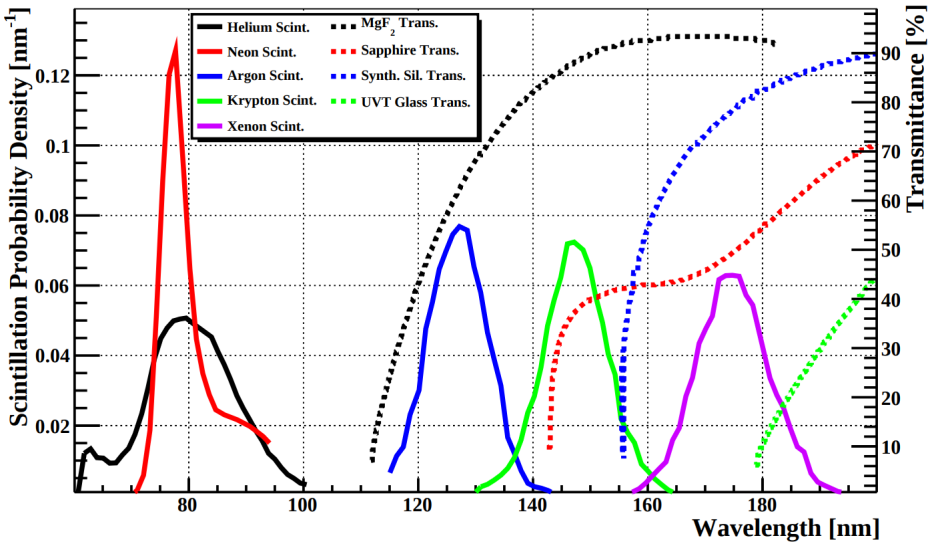


FIGURE 2.4: The scintillation spectra of several noble elements along the transmitance of the most common optical window material. [24] For the left axis in solid lines, *Helium* is shown in black ([25]), *Neon* is shown in red ([26]), *Argon* in blue, *Krypton* in green and *Xenon* in purple ([27]). For the right axis in dotted lines, $MgF_2$ is shown in black, *Sapphire* is shown in red, *Synthetic Silica* is shown in blue and *UV-Transmitting Glass* is shown in green. ([28], figure 4.5)

The more common solution to this issue is the use of *WLS* (*Wavelength Shifters*). Those compounds are capable of absorbing light in the VUV spectrum and re-mitting it in a less energetic region, where ordinary photodetectors are capable of detecting it. The most used WLS in combination with LAr is TPB (*TetraPhenyl Butadiene*).

The light conversion ability of TPB relies on the excitation process, where a photon is absorbed and excites an electron to a higher singlet state $(S_n)$ of the TPB molecule. This state decays radiationless to the lowest excited state $(S_1)$, where a radiative decay to the ground state produces the photon. This process has a characteristic time of the order of nanoseconds. The same mechanism is active in many other WLS such as pTP (*p-Terphenyl*) and BisMSB (*1,4-Bis(2-methylstyryl)benzene*).

### 2.2.1 Ionization of TPB

While exposed to high energy photons, other mechanisms could also play a role in the behavior of those compounds. Some authors suggested that the LAr VUV photons have enough energy to ionize the WLS molecules, where scintillation photons have energy around 9.4 $eV$ and the ionization potential of many compounds lies between 7 $eV$ and 8 $eV$. [23]

This mechanism is interesting due to its capacity of explaining not only observed discrepancies in LAr physics mentioned in 2.1.3, but also intriguing results on *greater-than-100%* efficiency measurements of TPB.

In this scenario, the ionized electron has enough energy to excite $S_n$ and also $T_n$ (excited triplet states) of surrounding molecules. The electron-ion pair recombination can also occur, producing $S_n$ and $T_n$. The $S_n$ decay in the same way described before, while $T_n$ has a different decay mode. The triplet states first undergo a very fast radiationless decay to the lowest excited triplet state ($T_n \rightarrow T_1$), where it is forbidden by selection rules to make the transition to $T_1 \rightarrow S_0$.

Although $T_1$ is forbidden to directly decay to the ground state, it is able to participate to triplet-triplet interaction. The interaction $T_1 + T_1 \rightarrow S_1 + S_0$ permits triplet states to decay into the ground state, although this process occurs in a much longer time scale.[29] The time profile can be calculated using the diffusion equation to estimate the diffusion of triplet states trough the material. This results in a non trivial behaviour that can be observed in equation 2.5, combined with a fast exponential component to account the singlet decays.

$$E(t) = Q_f \times e^{(-t/\tau_f)} + Q_s \times \frac{\eta_S N}{\left[1 + A\ ln\left(1 + t/\tau_s\right)\right]^2 \left(1 + t/\tau_s\right)} \tag{2.5}$$

Where $\tau_s$ and $\tau_f$ are the slow and fast constants of decay, respectively. $A$ and $N$ are constants that depend on the material. $\eta_S$ is the scintillation yield. $Q_s$ and $Q_f$ are the intensity of each scintillation mode.

With this reasonable assumption, it is possible to see clearly how TPB can present an efficiency greater than 100%. By ionizing the molecule, one incident photon can produce more than one scintillation photon through electron-ion pair recombination and excitation of other molecules caused by the ionized electron.

Also, it is possible to explain the appearance of a tertiary component in the liquid argon time profile. As TPB is used in combination with LAr, its time profile has to be taken into account as well. The longer time scale of the triplet-triplet interactions produces another component to the signal waveform, possibly with non-trivial time structure.

# Chapter 3

# Experimental tests on Wavelength Shifters

In the previous chapters, many aspects of the wavelength shifters were discussed. Its importance in the modern detectors was explored, showing that wavelength shifters make up the core part of all photon detection systems for DUNE. It was also highlighted that, despite having a good understanding of this compounds, some properties are not well known and others are not totally understood.

Due to its *hard-to-study* nature, the molecular properties of these compounds were tested indirectly, using different experimental approaches. In this chapter, these measurements on Wavelength Shifters characteristics will be reported.

## 3.1 Experimental approaches at WLS functioning

Wavelength shifters present many properties, e.g., total light yield, time emission pattern, photoemission spectrum.

It is possible, in fact, to understand the function mechanism of this compounds by measuring this properties, since they are both intimately connected. As an example, measurements on the temporal emission pattern provides a direct probe into the molecular ionization effect. While measurements on the relative

efficiency between the compounds provides a start on the understanding of how the ionization effect can interfere with the total efficiency of these compounds.

To properly measure some properties of this compounds, a delicate setup is needed. Precise excitation sources combined with fast and accurate light detection equipment are mandatory. Performing measurements with excitation in the VUV range adds a new difficulty in the setup, the measurements have to be done under high vacuum to allow the VUV light to propagate.

The samples used in every measurement have to meet a high consistency standard to ensure reliable results. Samples of the wavelength shifters of interest are not commercially available, making the *in-lab* production mandatory. A careful procedure was conceived to produce high quality samples, using the vacuum evaporation technique. To ensure the expected quality, several quality control steps were performed with the produced samples, which included measurements of thickness, surface density, surface roughness, surface crystalline structure and emission spectrum. All this processes are discussed in depth in the appendix A.

## 3.2 Temporal Emission studies

The emission pattern of a wavelength shifter is tightly bounded to the molecular excitation processes, as it was discussed in chapter 2. In the simplest case only the singlet states would be excited, resulting in a emission with a time constant $\tau_{fast} \approx 1\ ns$. Considering the hypotheses of ionization of these molecules, the triplet states could also be excited, resulting in a decay with a much longer time constant, in the order of several microseconds. Observing the time emission spectrum of this compounds gives a good way to test not only the standard singlet state excitation but also the ionization hypothesis. Therefore a set of measurements of this feature was planned. In sections 3.2.1 a detailed discussion on the setups and methods used is presented.

### 3.2.1 Single Bunch at LNLS

The purpose of this set of measurements was to investigate the wavelength shifters' time emission spectrum by measuring its response to excitation light in the range of the noble gases emission. To properly measure it, a precise light source ranging from 6 $eV$ up to 15 $eV$ is desired, in order to cover the emission spectrum of all noble gases used in particle detection. This light source has to be pulsed with a small pulse width and a long period between pulses. This is needed so the pulse shape does not interfere in the response and the delayed emission response has enough time to evolve.

Light sources that meet all the requirements are not common. Nonetheless, the *Toroidal Grating Monochromator* (TGM) Beamline at *Brazilian Synchrotron Light Laboratory* (LNLS) was designed to operate in that regime. [30, 31]

Situated in Campinas, the *LNLS* provides a good infrastructure to many measurements using Synchrotron Light. The *UVX* light source is equipped with 17 experimental stations, capable of operating from infrared to x-rays with great energy precision. The *TGM* Beamline is one of the experimental stations of the *UVX* at *LNLS*. Capable of operating from 3 $eV$ up to 330 $eV$ and providing a suitable infrastructure, the TGM is an optimal site for this measurements. It's whole structure is periodically tested and calibrated. Moreover, the TGM has been used by many research groups, where more than 145 scientific papers were produced, further assuring its high reliability level. Its beam line, held in ultra high vacuum, is instrumented with several filters to ensure the light purity. A picture of the beam line can be observed in figure 3.1.

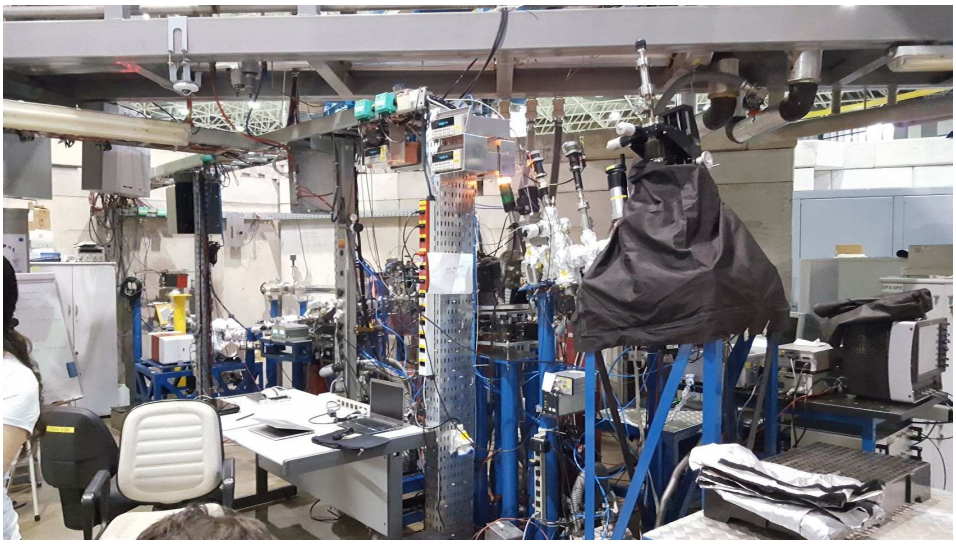

FIGURE 3.1: A picture of the layout of the Toroidal Grating Monochromator line. In this picture is possible to observe from the beam source (the bending magnet exit) on the background all the way until the experimental chamber, in the foreground.

Its experimental chamber is equipped with an adjustable sample holder, capable of positioning different samples into the beam. The chamber is instrumented with a *Hamamatsu r928* photomultiplier tube (PMT), connected though an optical fiber. It also provides several accesses to install more photodetectors.

In the *UVX*'s normal operation (*multibunch mode*), the *TGM*'s light waveform does not offer a long enough period between pulses to observe the delayed components. Nevertheless, the *UVX* is also capable of operating in *Single Bunch mode* which provides a fast 150 $ps$ pulse with a much longer period between pulses $(300\ ns)$.

It is not common for a synchrotron light source to operate in this manner, due the fact that many experimental lines do not benefit from that operation mode. The singular scheduled *Single Bunch mode* operation of the *UVX*, in September 2016, provided the opportunity to make this measurements using this ideal setup. Our group was granted two days of beam time, where the measurement's setup was set using the *TGM* line operating in the range from 7 $eV$ to 10 $eV$. This range

was chosen due the transmittance of the $MgF_2$ filter used to suppress higher order resonances. A *Hamamatsu r11065* PMT was installed directly into the chamber, to be able to capture maximum light. Both PMT's were connected to a fast *Analog to Digital Converter* (ADC), so the average waveform could be acquired. An illustration of the setup is depicted in figure 3.2.

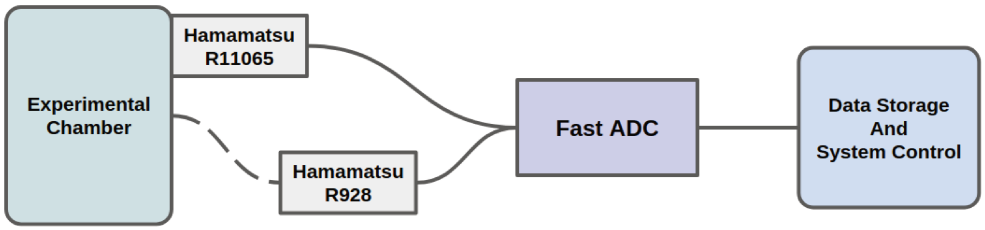


FIGURE 3.2: Schematic representation of the setup used in the measurements. The dashed line connecting the photodetector to the experimental chamber represent an optical fiber.

For each wavelength shifter of interest, several samples were produced with the most common thickness and substrates. A picture of the populated sample holder, after the measurements, can be observed in figure 3.3.

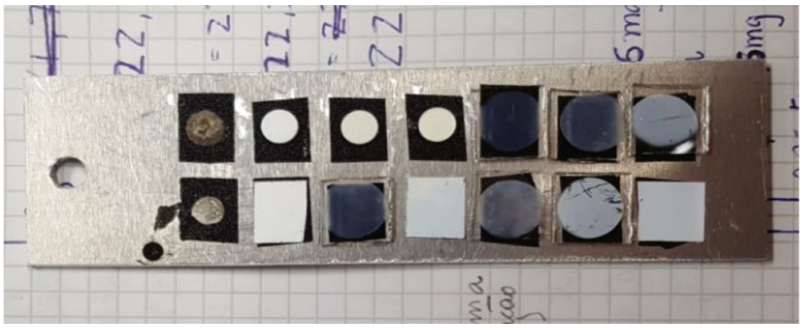

FIGURE 3.3: Sample holder used in one of the measurements. This picture was taken after the measurements were performed in order to not expose the samples to the ambient light.

The WLS used in this tests were *TPB*, *pTP*, *BisMSB*, *POPOP* and *PPO*. All the samples used were manufactured at UNICAMP.

The measurements proceeded by acquiring $10^4$ waveforms per excitation light energy, followed by a dark measurement. This was done to inspect any stray light in the system, which could interfere with the results. This measuring routine was applied for every sample. For each measurements, a mean waveform was stored in the system.

After all samples were measured, a direct reflection of the beam was measured.[1] This is done to measure the photodetector's IRF (*Impulse Response Function*). The beam's pulses are fast enough to be treated as a delta impulse, and so the measured waveform corresponds to the detectors impulse response function by definition. A detailed explanation on this subject can be found in appendix B.

To analyze the data, a *ROOT toolkit* based software was created. It is designed to work in steps, being composed of four *ROOT macros* and a main program written in *bash* language.

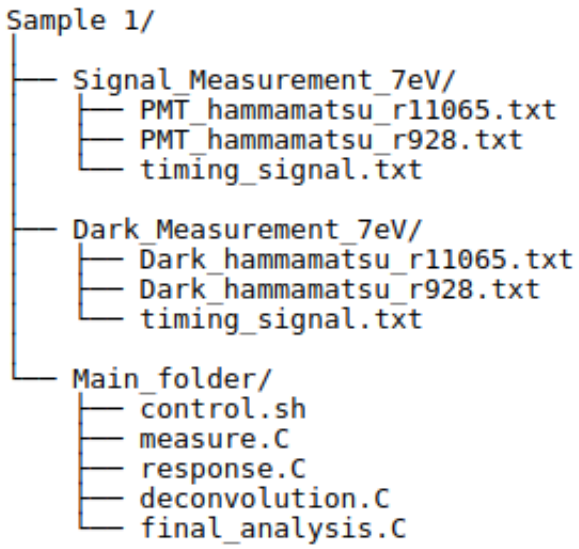


FIGURE 3.4: The layout of the folder to analyze the data with the automatic software. In this example, the sample 1 was measured with only one excitation wavelength for simplicity.

[1]This was performed by shining beam into the aluminum sample holder with the beam in a wavelength that the photomultipliers were able to read.

With the measurements organized in a folder, as seen in figure 3.4, the software is executed in it. The bash main program is responsible to run the analysis' macros inside the desired sub-folder, to extract and to organize the final results. The macros are designed to control specific analysis tasks,

- Read the measurements and detector response files, subtract the background and wright the data to a *ROOT Tree* file.
- Perform the deconvolution process. The resulting signal is fitted with the expected WLS comportment. The fit data is saved in a text file.
- Reads the fit text file from all the measurements and produces the plots for all the samples.

At figure 3.5 it is possible to observe the first result of this analysis. The measured waveform, the response function and the deconvoluted data for a TPB sample excited with 9 $eV$ photons. The deconvoluted data is fitted with a function that models its behaviour, discussed in 2.2.

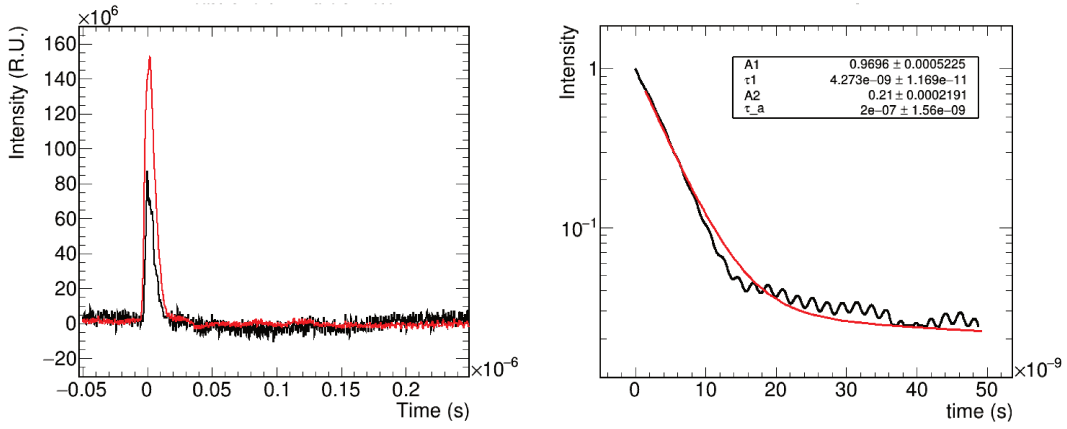


FIGURE 3.5: At the left it is presented the measured signal (red) on top of the measured IRF (black). At the right it is possible to observe the deconvolution result.

For each sample, this step was performed for every measurement and the fit parameters were stored in a text file. After that, all data were compiled in one

graph of several fit parameters versus wavelength, as is shown in figure 3.6. The fit used is based on the equation 2.5, which describes the systems behaviour. It is implemented as shown in equation 3.1.

$$E(t) = S_f\, e^{(-t/\tau_f)} + S_s\, \frac{\eta_S N}{\left[1 + A\, ln\,(1 + t/\tau_s)\right]^2 (1 + t/\tau_s)} \tag{3.1}$$

Where the parameters $S_{fast}$ and $S_{slow}$ represent respectively the intensity of the fast and slow component in the signal. $A$ and $N$ are parameters that depends on the scintillator material and $\tau_{fast}$ and $\tau_{slow}$ represent the time component of each decay type.

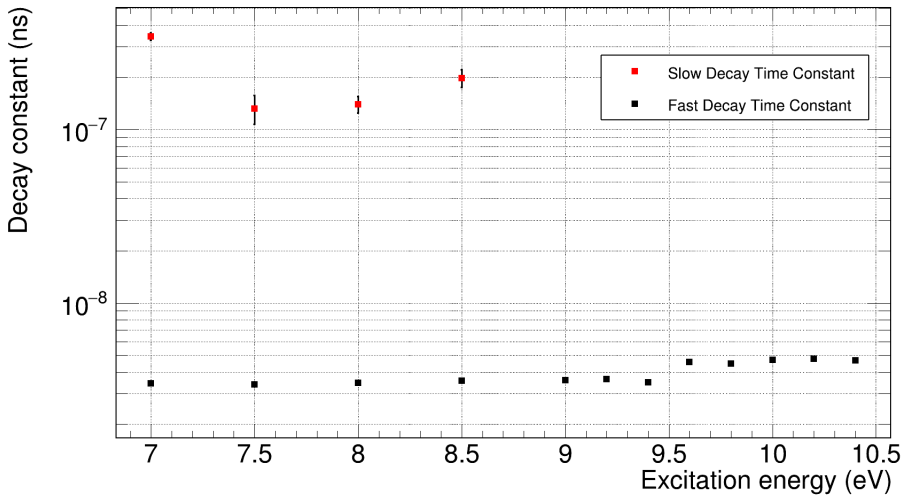


FIGURE 3.6: In this graph it is possible to observe the fast (black squares) and slow (red squares) decay component of a TPB sample versus the excitation wavelength. It is possible to observe that this stays almost constant until 9.5 $eV$, where the signal strength is too low for the deconvolution to work properly.

This analysis was performed for every sample and the most relevant results shown in table 3.1,

| | $S_{fast}$ | $\tau_{fast}$ $(ns)$ | $A$ | $S_{slow} \times \eta_s N$ | $\tau_{slow}$ $(ns)$ |
|---|---|---|---|---|---|
| TPB − tablet | 0.95 | $5.59 \pm 0.05$ | $0.333 \pm 0.001$ | 0.05 | $89.2 \pm 18.4$ |
| TPB − VM2000 | 0.97 | $3.98 \pm 0.03$ | $0.283 \pm 0.001$ | 0.03 | $203.8 \pm 19.4$ |
| TPB − VM2000 | 0.96 | $4.07 \pm 0.02$ | $0.385 \pm 0.001$ | 0.04 | $239.4 \pm 32.2$ |
| Sodium Salicylate | 0.93 | $9.1 \pm 0.1$ | $0.210 \pm 0.001$ | 0.07 | $10.1 \pm 0.1$ |

TABLE 3.1: In this table the most relevant measured parameters of each sample are presented. The parameters rise from the fit equation 3.1.

One notable result is the close agreement of the measured time components of the *Sodium Salicylate* with the literature, where the fast and slow components are shown to be 8.5 $ns$ and 10 $ns$, respectively. [32] This results present a confirmation of the method used in this analysis, where it not only agrees with the previous measurements but also measures the quantities with more precision.

Other important result is the close agreement between the measured and literature values of the TPB tablet sample delayed light properties, where $t_{slow}$ is shown to be 51 $ns$ and $A$ is shown to be 0.22.[23]

The results, although partially different than the ones found in the literature, show a clear indication of the ionization process in the most common wavelength shifters used in combination with liquid noble gases detectors. There are many relevant effects for the experiments that rise from this confirmation and more measurements have to be performed to fully understand the effect.

## 3.3 Relative efficiency measurements

One important aspect of the ionization effect is how it alters the wavelength shifting efficiency of this compounds. The most common way of quantifying the efficiency of WLS is to divide the number of converted photons by the number of

incident photons. However, the possibility of producing more then one low energy photon for each high energy photon implies that the method of quantifying the efficiency can imply an efficiency higher than *100%*. [24] This presents a contradiction in the method, where using the ratio of produced photons by number of incident photons as efficiency produces nonphysical results. It also affects the energy resolution of the photodetectors used, since the error is associate with the square root of the number of incident photons. If more than one produced by the wavelength shifter for each incoming photon, the error would be overestimated.

In the following section, measurements of relative efficiency of WLS when irradiated by *UV* and *VUV light* will be reported. This will explore the first step in the understanding of how the ionization can affect the efficiency.

### 3.3.1 TGM at LNLS

The purpose of this set of measurements was to properly measure the relative efficiency of different wavelength shifting compounds, using a calibrated light source in a well established and reliable setup. For these reasons, the TGM beamline at LNLS was chosen. It was stated in previous discussions that the TGM beamline in an optimal site to measure the properties of WLS due its reliable infrastructure, fitting excitation range with high energy resolution ($\Delta E \approx 0.02\,eV$ at $10\,eV$) . Using TGM's synchrotron light as excitation source for this tests allows the relative efficiency to be measured for several wavelengths, due to its ability to operate at a wide spectrum.

The TGM line was used with the UVX operating in the *multi bunch mode*, providing an almost continuous beam. The excitation range was selected to cover the emission spectrum of most common noble gases, shown in figure 2.4. Setting the range from $6\,eV$ up to $10\,eV$. To achieve this range while maintaining the higher

order resonances suppressed, a *magnesium fluoride* ($MgF_2$) filter was installed in the beamline.

The sample's emission was monitored using the same setup described in figure 3.2. A *keithley 6514 picoammeter* was used to acquire the PMT's current, and the data was stored using the TGM's software. an illustration of the experimental setup can be seen in figure 3.7.

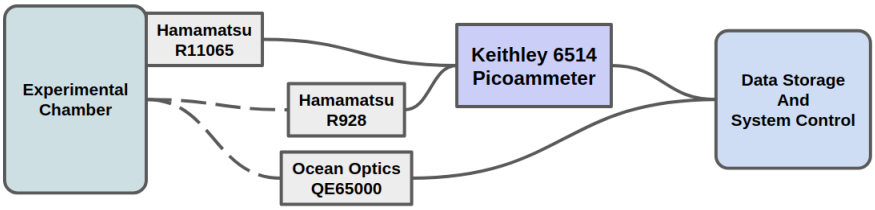


FIGURE 3.7: In this figure, it is possible to observe a schematic representation of the setup used in the measurements. The dashed lines connecting the photodetectors to the experimental chamber represent an optical fiber.

The beam measurements consisted in illuminating the sample with the monochromatic light provided by the TMG's monochromator, while measuring the light emitted by the sample using the photomultipliers and the picoammeter. This was performed for several wavelengths inside the established range, with a 0.1 $eV$ step between different wavelengths.

The experimental procedure was to perform the beam measurement for each sample followed by a background check, which consists in measuring the current in the PMTs with no beam in the chamber. The procedure was conceived to minimize the time between two measurements and reduce the effects of eventual fluctuations in the beam intensity. In fact, the synchrotron light intensity presents a slow exponential decline over time combined with a small non trivial behaviour. Making the comparative measurements quickly allows to minimize these effects.

After performing all intensity measurements, the emission spectrum of every sample was also measured, using an *Ocean Optics QE65000* spectrometer. This step was important to properly correct the intensity measurements, due to the fact that the PMT's *Quantum Efficiency* (QE) will alter the efficiency measurement by a factor which is equal to the average of the emission spectrum over the PMT's QE.

To analyze the data from the emission spectrum measurements, another *MATLAB toolkit* based software was designed. It produces a PE spectrum for each excitation wavelength. One example can be seen in figure 3.8.

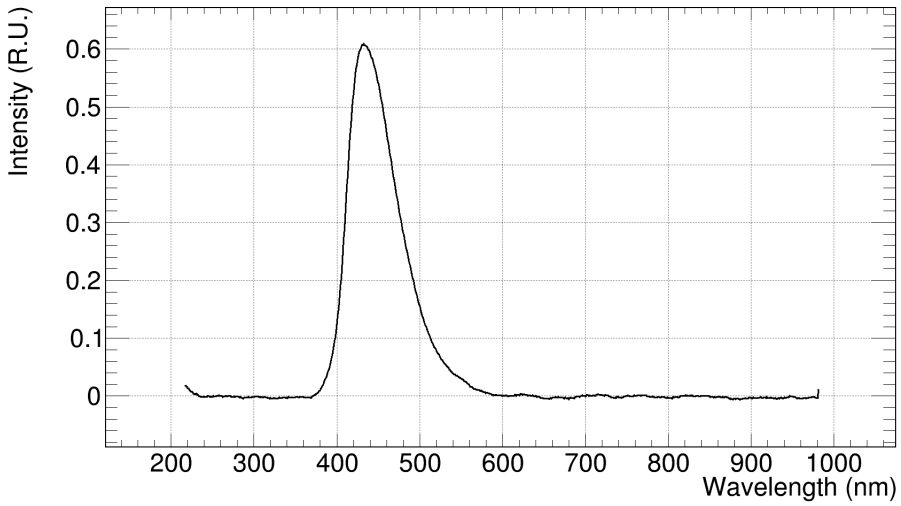


FIGURE 3.8: The measured emission spectrum of a TPB sample when irradiated with 9 $eV$ light.

For the intensity measurements, the data analysis requires several steps, since the measured intensity depends on several parameters, as shown in equation 3.2. A *MATLAB toolkit* based software was implemented to analyze the data.

$$I^m(\lambda) = I_0(\lambda) \times F(\lambda) \times f_{\,solid\ angle} \times I_{sample}(\lambda) \times P + B(\lambda), \tag{3.2}$$

where $\lambda$ is the excitation wavelength, $I_0$ is the beam intensity, $I^m$ is the measured intensity, $F$ is the filter transmittance, $f_{\,solid\ angle}$ is a parameter that depends on the geometry of the detectors and sample, $I_{sample}$ is the true sample response, $P$ is the PMT's QE correction and $B$ is the background.

The software's first step in the analysis is to remove any free parameters from the samples' *photoluminescence* (PL) spectrum. Subtracting the measured background and dividing the measured PL spectrum by the ring current, the contribution from $B$ and $I_0$ vanishes due that $I_0$ is predominantly proportional to the ring current.

In the next step it divides two PL spectra, removing the contribution from $F$ and $f_{solid\ angle}$. Since only temporarily close measurements are compared, any residual time depended contribution from $I_0$ is also removed. By rearranging the terms, as seen in equation 3.3, it is possible to obtain the relative efficiency measurement.

$$\frac{I_{sample\ 1}(\lambda)}{I_{sample\ 2}(\lambda)} = \frac{I^m_{sample\ 1}}{P_{sample\ 1}} \times \frac{P_{sample\ 2}}{I^m_{sample\ 2}} \tag{3.3}$$

The result of the software at this step is a graph of relative efficiency versus excitation wavelength. One example can be seen in figure 3.9.

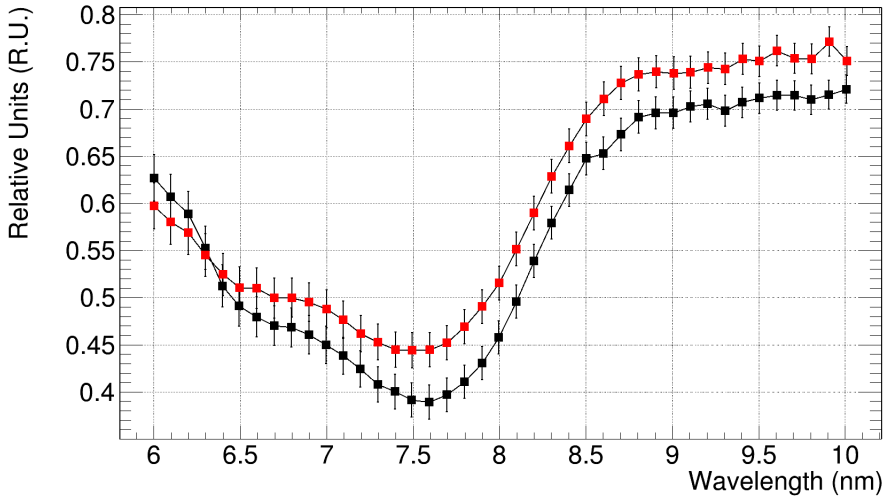


FIGURE 3.9: The relative PL spectrum between samples. The two lines represent different BisMSB samples relative to the same TPB sample, where the difference is the thickness of the BisMSB samples. In red it is depicted the PL spectrum for a 15.3 $\mu m$ BisMSB sample relative to a 14.1 $\mu m$ TPB sample. In black is depicted the PL spectrum for a 21.3 $\mu m$ BisMSB sample relative to a 14.1 $\mu m$ TPB sample.

This analysis was performed for every sample measured, resulting in many relative PL spectra. This analysis represent a first step in the understanding of efficiency effects due the ionization process, and more measurements have to be performed to fully understand this effect.

Using the data collected it was possible to perform an analysis of how the efficiency of TPB changes with its thickness when exposed to LAr scintillation light. This is an important measurement for any detector that uses TPB in combination with Liquid Argon and can be found in the literature. [33] The results of this analysis are show in figure 3.10.

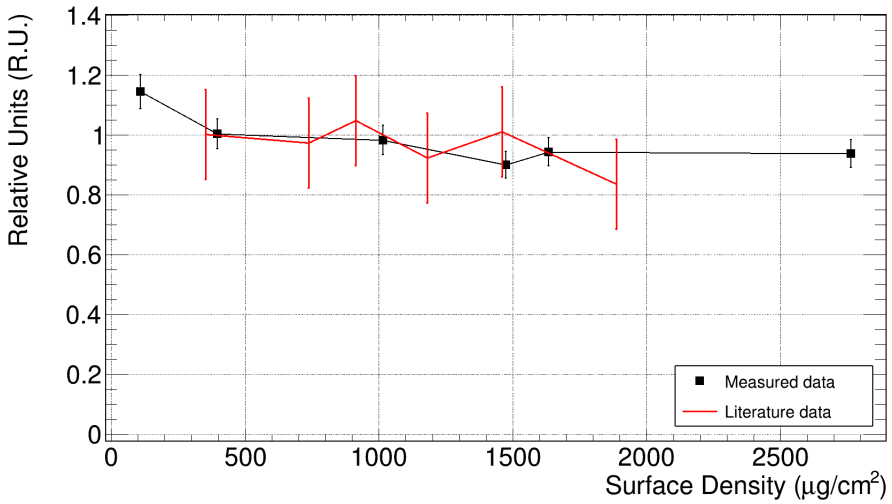


FIGURE 3.10: A graph of the relative efficiency of different TPB samples for several sample thickness, shown in black squares. The results from the literature are pictured in red. [33]

It is possible to observe that the results from this analysis not only are in agreement to the ones found in the literature but also extend the range measured with grater precision.

# Chapter 4

# Optimization of Arapuca Efficiency

One important aspect to consider when designing a photodetector is its efficiency. The efficiency of this detector will be composed by the efficiency of its components. When using WLS in a detector, it is fundamental to choose the right WLS compound so it will operate in the region that maximizes its efficiency. For example, the ARAPUCA working principle foresees the use of a combination of two different shifters, one for converting the 128 nm LAr scintillation light and the other to trap the photons inside its reflective cavity. The matching of the emission and absorption spectra and efficiencies of the two compounds is important for the final detection efficiency.

In this chapter, several measurements on WLS relative efficiencies will be presented.

## 4.1 TGM at LNLS

As discussed before, the TGM beamline at LNLS is an optimal site to measure the properties of WLS due its appropriate infrastructure. Using TGM's synchrotron light as excitation source for these tests allows the relative efficiency to be measured for several wavelengths, on account of the TGM's precise monocromator.

In this set of measurements, the TGM beamline was used with the UVX operating in the *multi bunch mode*, providing an almost continuous beam.

In this measurements, the excitation range was selected so it covers the most common WLS's emission spectrum, which addresses the most common combination of wavelength shifters.

To achieve this broad range while maintain the higher order resonances suppressed, three different filters had to be used. The range was splitted into 2 smaller regions, where each filter presents a high transmissivity. The filters used were common glass and fused quartz. They where used, respectively, in the regions 3 $eV$ to 5 $eV$ and 4.5 $eV$ to 8 $eV$.

The experimental setup used in this set of measurements closely matches the one used in the section 3.3.1, pictured in figure 3.7, as it is an extensively tested and a regularly calibrated setup, used by many groups in the TGM beamline.

The experimental procedure was to perform the beam measurement to each sample followed by a background measurement, which consists in measuring the current in the PMTs with no beam in the chamber.

To study the sample degradation effect, long measurements were also performed. They consisted in irradiating a desired sample with a sequence of monochromatic light for a long time while recording the response intensity.

To analyze the data taken from the long measurements, a simple *MATLAB toolkit* based software was designed. It produces a graph of intensity over time, normalized to the first point in the graph. One example can be seen in figure 4.1.

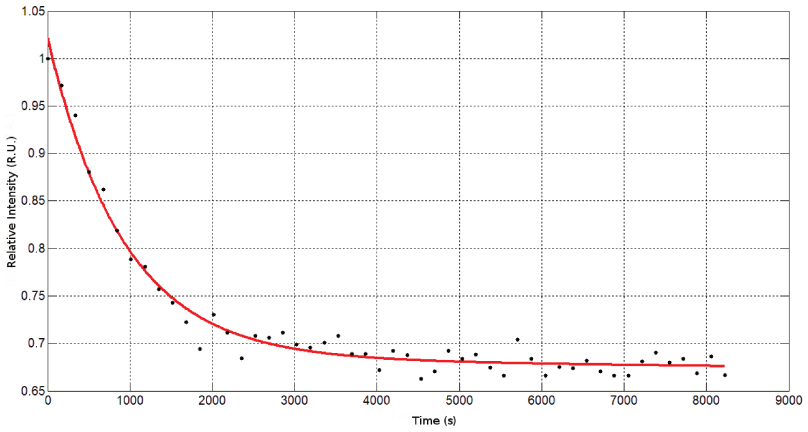


FIGURE 4.1: The relative intensity versus time graph for a pTP sample. A two exponential fit, $f(x) = Ae^{(\tau_a x)} + Be^{(\tau_b x)}$, was performed. It shows that the fastest decay constant, $\tau_a^{-1} = 17\ min \pm 3\ min$, is much bigger than the measuring time, $O[1\ min]$.

The analysis of the the intensity measurements was performed in the same way as described in section 3.3.1, where first the measured background is subtracted to the samples' photoluminescence spectrum and then divided by the ring current. Then the two PL spectra of interest are divided, removing the contribution from any non time correlated systematic, e.g. the filters transmissivity or the detectors solid angle. This produces a relative PL spectrum of two samples of interest, which is independent of the setup. One example of this can be seen in figure 4.2.

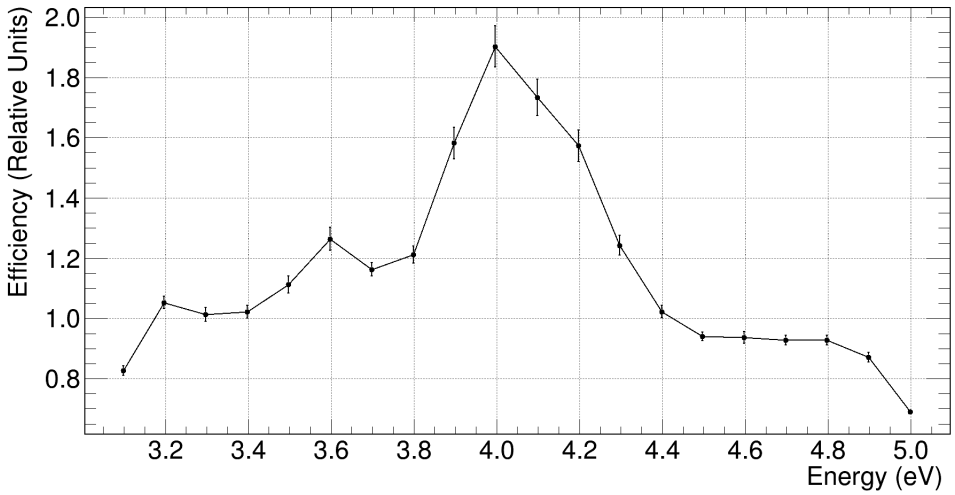


FIGURE 4.2: Relative efficiency of two TPB samples versus the excitation wavelength.

The software's last step is to average the relative efficiency spectrum over the emission spectrum of a noble gas or a WLS. This is done so the final result will be a relative efficiency value for a particular sample when illuminated by a certain spectrum. In this way, different samples can be easily compared and it is possible not only to investigate the best wavelength shifter for each application, but also the best thickness, best substrate or any other property. In figure 4.3 it is possible to observe a graph of TPB's relative efficiency versus sample thickness when averaged over pTP emission spectrum.

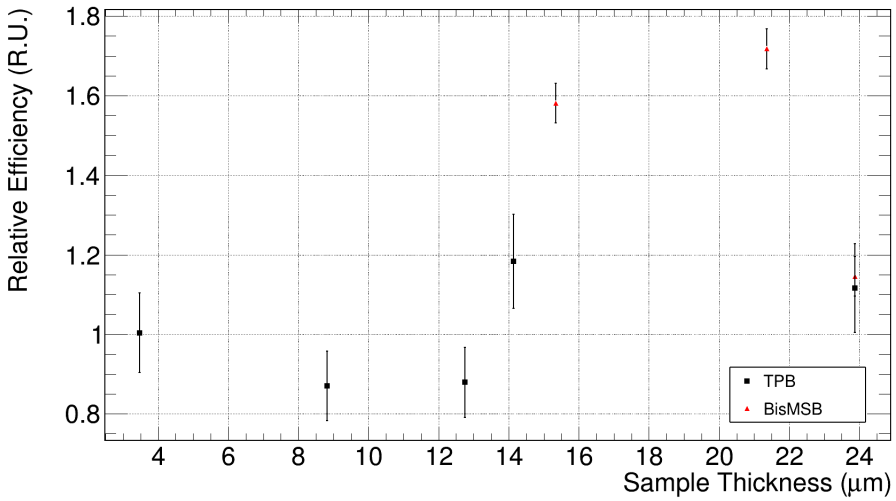


FIGURE 4.3: The relative emission efficiency of several samples of TPB (black) and BisMSB (red) versus thickness, when illuminated by pTP light.

Many results were produced for several wavelength shifters, with different thickness and substrate. In particular, a result of this analysis, shown in figure 4.3, presents a behaviour never reported in the literature. Some samples of BisMSB show a higher efficiency than all TPB samples when illuminated by pTP light. This is an important hint due the possible application on the optimization of the efficiency of the ARAPUCA device.

More measurements have to be done to understand how this higher efficiency behaves for different sample thickness. In the next section, more measurements on this subject will be discussed.

## 4.2 TUM measurements

As a confirmation test for the hints found in the LNLS measurements, a measurement plan was scheduled at the TUM university (*Technische Universität München*) in Munich. Am *Agilent Cary Eclipse Fluorescence Spectrophotometer* was used for the

measurements. This equipment is capable of performing fast and accurate measurements in the UV-Vis range, with several filters to ensure the spectral purity. Consequently, this is an ideal setup for the intended measurements.

Several samples of BisMSB and TPB were measured using this setup, with thickness ranging from 180 $\mu g/cm^2$ to 1060 $\mu g/cm^2$. For each measurement, the spectrometer returns a PE spectrum for every excitation wavelength used. This is shown in figure 4.4.

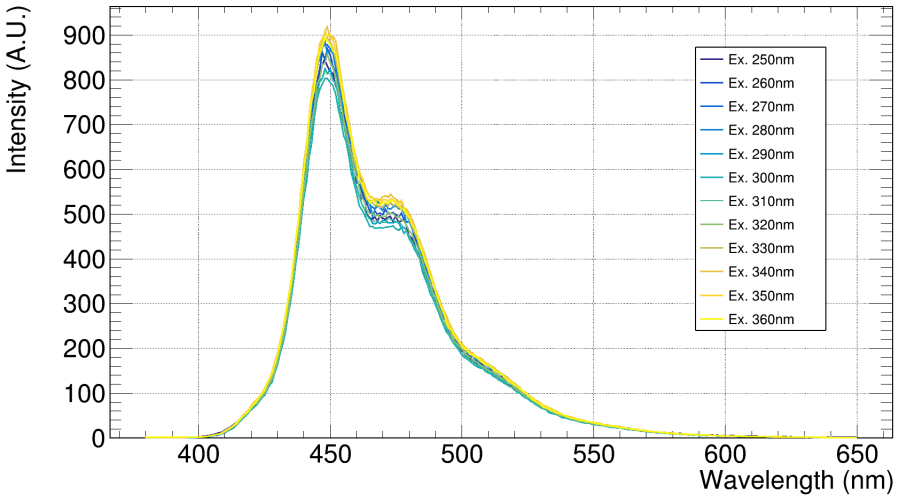


FIGURE 4.4: A graph of the photoemission spectrum measured of 497 $\mu g/cm^2$ BisMSB sample, for several excitation wavelengths.

These spectra are integrated to produce an intensity value for each excitation wavelength, resulting in a PL spectrum for each sample. After obtaining the PL spectrum for each sample, the same data treatment as the one used in the LNLS relative measurements was applied. First the PL spectra were divided by a PL spectrum from a reference sample, to produce a relative PL spectra. Then, the relative spectra were corrected by the pTP emission, to produce a relative efficiency value for each sample. This result is shown in figure 4.5.

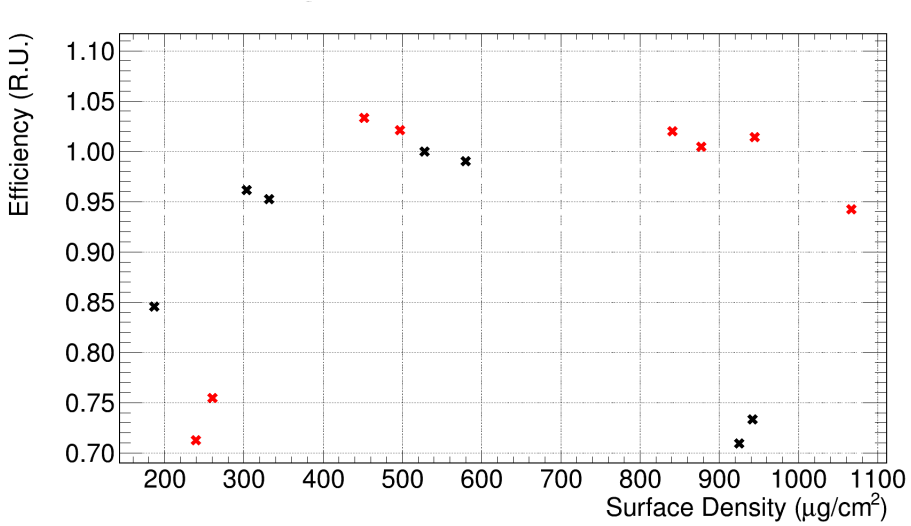


FIGURE 4.5: A graph of the relative efficiency of several samples of BisMSB (in red) and TPB (in black) for different sample thickness.

It is possible to see that, as suggested by the hint obtained in the LNLS, that for the commonly used thickness BisMSB is more efficient than TPB when illuminated by pTP light.

The difference in efficiency is not big enough for a relevant efficiency increase of the ARAPUCA device. However, this is still an important result for the device, as the cost of BisMSB is approximately three times lower than TPB, which can further decrease the cost of the detector. [34, 35]

To properly study how this new wavelength shifter will perform in an real detector, new measurements have to be done. These measurements will be discussed in the next section.

## 4.3 Dark Box tests

The measurements using monochromatic light are ideal to quickly test many samples over a large range of the wavelengths. Concerning the ARAPUCA's

efficiency, other methods can be used. By constructing an ARAPUCA with *easy-to-change* interior and exterior WLS it is possible to test its efficiency for many different combinations.

In this test, an ARAPUCA with easily interchangeable wavelength shifters was made. Its design is displayed in figure 4.6.

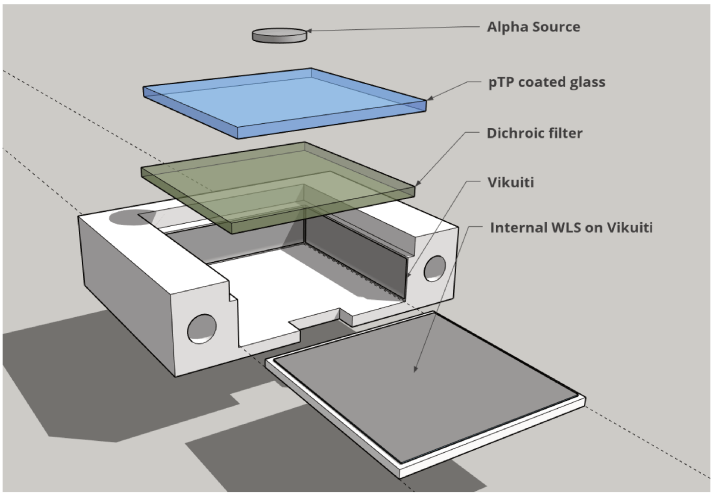


FIGURE 4.6: An exploded view of the ARAPUCA design with *easy-to-change* WLS.

To excite the exterior WLS, a natural Uranium alpha source was used. A 400 *nm* cutoff dichroic filter was used to produce the ARAPUCA effect. The light was collected using an *ETL D*750 PMT which was coupled to the side of the detector. To acquire the pulse shapes, a *DT*5720*B CAEN digitizer* ADC was used. The data was acquired and stored in a computer using the CAEN *Wave-Dump* software. The whole apparatus was operated inside a dark box to prevent ambient light to damage the PMT and interfere in the result.

The measurements where done for several samples of BisMSB and TPB as internal wavelength shifters. By varying its thickness it is possible to find not only the best wavelength shifter for this application, but also the best thickness.

A modification of the apparatus also allowed to install a light guide inside, an so to test the X-ARAPUCA's efficiency, which was described in section 1.2.2.

To analyze the data, a *ROOT toolkit* based software was developed. It reads and integrates the acquired waveforms to produce the pulse charge. After this, it fills an histogram of pulse charges and proceeds for the next waveform. An example of this analysis can be seen in figure 4.7, where the conversion between the number of photons and the ADC counts was made by finding the single photoelectron charge in ADC counts dividing the X axis by this value.

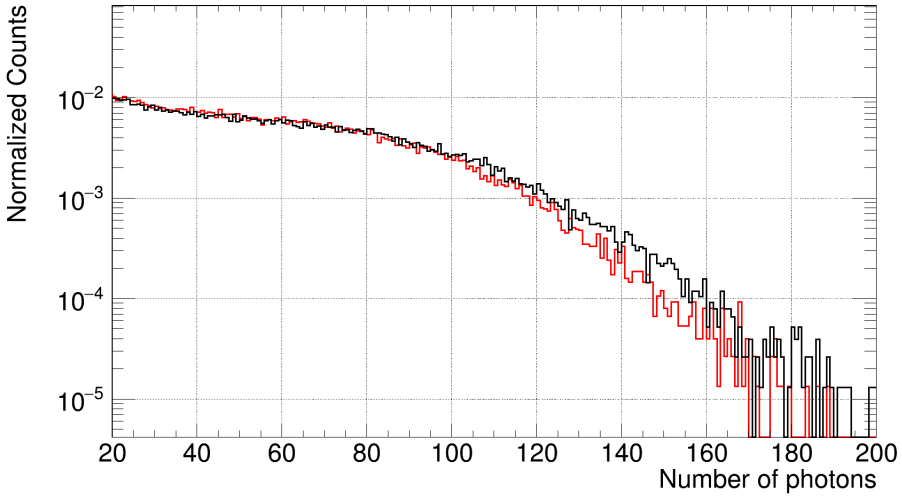


FIGURE 4.7: The histogram of number of photons for the most efficient samples of TPB (in red) and BisMSB (in black) as ARAPUCA's internal shifters.

To produce a relative efficiency value from this data, a *chi-square* minimization between the histogram of the samples has to be performed. It consisted in implementing two scale parameter into a histogram, one for each axis. This parameters were adjusted so the *chi-square* between both histograms is minimum. This was performed using the *TMinuit* library from the *ROOT toolkit*. This can be seen in figure 4.8.

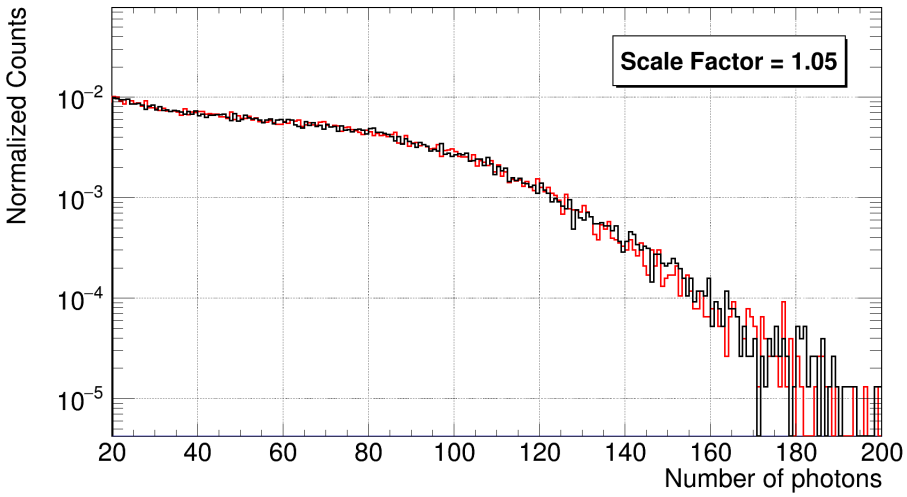


FIGURE 4.8: The scaled histogram of figure 4.7, where a scale factor was used in the TPB histogram to adjust it to the BisMBS histogram.

The scale factor was found to be 1.05 which implies that this sample of BisMSB is 5 percent more efficient than the TPB one, which is compatible with the data found in the TUM measurements. This further confirms the advantage of using BisMSB as the internal wavelength shifter in the ARAPUCA device.

# Chapter 5

# ARAPUCA and X-ARAPUCA Monte Carlo Simulation

In this chapter, a comparison between the X-ARAPUCA device, described in section 1.2.2, and the ARAPUCA will be approached though the use of Monte Carlo simulations. Both devices will follow the design of the standard DUNE Supercell Module, respecting its imposed geometry and building materials. This not only permits to approach a real world situation with the correct materials but also allows many important tests of the DUNE standard PD module to be made. [3]

In conjunction, many parameters of the X-ARAPUCA device, described in section 1.2.2, will be tested to understand how this considerations affect the final efficiency of the device.

For this Monte Carlo simulation, the *Geant 4 toolkit* was used. This platform was chosen due to its extensive use in the particle physics field, which results in an ideal and scalable environment with most tools already implemented. [36] A functioning simulation code in *Geant 4* requires many steps to be defined. The most important steps in this code were the geometry construction, the physical processes and the data acquisition. This steps will be explained in the following discussion.

## 5.1 *Geant4* implementation

It was chosen to generate the LAr scintillation photons manually, to avoid the complex scintillation implementation and analysis. The photons were directed towards the optical window, where they interact with the device. As output, the simulation presents the efficiency of the detector, which is defined as the ratio of the number of photons which reaches the SiPM active area with the number of generated photons. The simulation is also capable of retrieving information any other information of the detected photon, for instance the time of flight and the detection position. This information allows the comprehension of the trapping mechanisms.

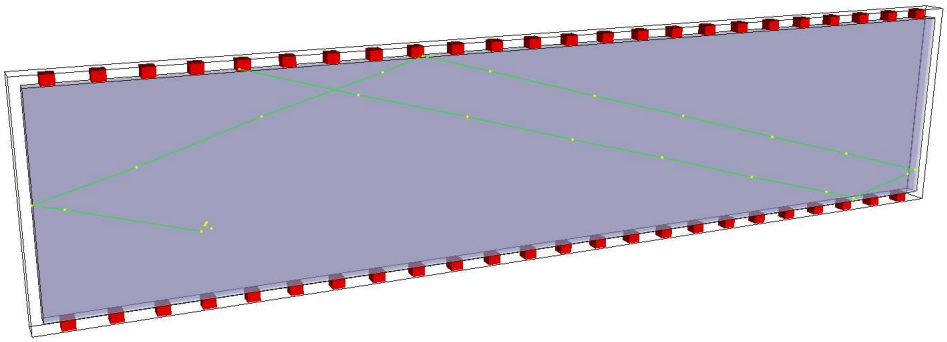

FIGURE 5.1: A picture of the simulation of one event on the X-ARAPUCA device. The internal dimensions of the device are $0.6\ cm \times 10\ cm \times 48\ cm$. The photon trajectory is seen in green and a yellow dot is placed at each step.

In figure 5.1 it is possible to observe the ordinary operation of the simulation, where a photon is generated outside the device and interacts with it. In this case, it is accepted through the optical window and is trapped inside, where it reflects until it is detected by one of the SiPMs.

In this simple case, the efficiency is unreasonable high with a corresponding high uncertainty, $100\% \pm 100\%$ , caused by the small number of simulated events.

To acquire trustworthy results, many events have to be simulated, as the error is proportional to the square root of the number of detections. For this reason, several optimization options were introduced in the simulation code to ensure a fast execution.

### 5.1.1 Geometry

The geometry implemented in the simulation is based on the design of the standard DUNE Supercell Module, which is accepted to be the standard photodetection system of DUNE. [3] The geometry was parametric constructed so that any dimensions could be easily changed, allowing other proportions to be tested, as it is discussed in section 5.3. The SiPMs were implemented using the *G4PVReplica* method, permitting an easy alteration of their quantity for any geometry.

FIGURE 5.2: A picture of a cross section of the geometry of the implemented X-ARAPUCA. It is possible to observe the dichroic filter in gray; the light guide bar in blue; the SiPMs in red; and the X-ARAPUCA body transparent with black edges. The external wavelength shifter can not be seen in this figure due to its small thickness in this scale.

In figures 5.2 and 5.1 it is possible to observe a cross section view of the implemented geometry, where the SiPMs are represented in red, the Light Guide Bar is shown in blue and the Dichroic Filter is pictured in light gray. The X-ARAPUCA body is transparent with black edges, this was done to allow an easy view of the internal structure of the detector.

The material used in the construction were *PTFE* for the X-ARAPUCA body; *Acrylic* for the Light Guide Bar, with an index of refraction of 1.5; *Fused Silica* for the SiPMs and the Dichroic filter, with an index of refraction of 1.5. The external wavelength shifter was constructed as a thin films made of *pTP*. The material used for the world was Liquid Argon, with a index of refraction of 1.23. For the ARAPUCA module, TPB was used as the internal WLS.

This geometry is implemented to closely follow the ideal design of the device. Nonetheless, the real technical drawing can present some differences, e.g., the clearance between the SiPMs and the bar the number of SiPMs and the wavelength shifters. All this factors will be tested to estimate how they can affect the efficiency of the device.

### 5.1.2 Processes

In *Geant 4* it is possible switch on and off several physical processes. In this implementation, only the optical processes were set to be active. This was done to achieve a high performance, allowing millions of events to be simulated in the order of a few minutes, which is essential to test several parameters.

The optical processes in Geant4 can be separated in two main categories, bulk and surface processes.

The bulk processes are defined as the processes that occur inside the material, e. g., refraction index related processes, wavelength shifting and bulk optical absorption. This processes were attributed to all light permeable materials in the simulation, with the exception of the Wavelength Shifting property. This was only implemented for the external Wavelength shifter and the Light Guide Bar.

The surface processes are defined as the processes that occur in the surface of the solids. These are surface reflection and the dichroic property of the dichroic filter. A reflective surface was implemented for the internal walls of the X-ARAPUCA,

with a set reflectivity of 95%. This value was obtained from the *data-sheet* of the reflective material that covers the internal walls of the detector. [37]

The implementation of the Dichroic property is done using the reflective surface class, were it can be implemented for several wavelengths. The data was obtained from the data-sheet of the dichroic filter.

Some implemented properties are seen in figure 5.3. It is possible to observe that the first wavelength shifters absorbs in a high energy region and reemits in a spectrum that overlays with the dichroic filter transparent region, as it was defined in the section 1.2.

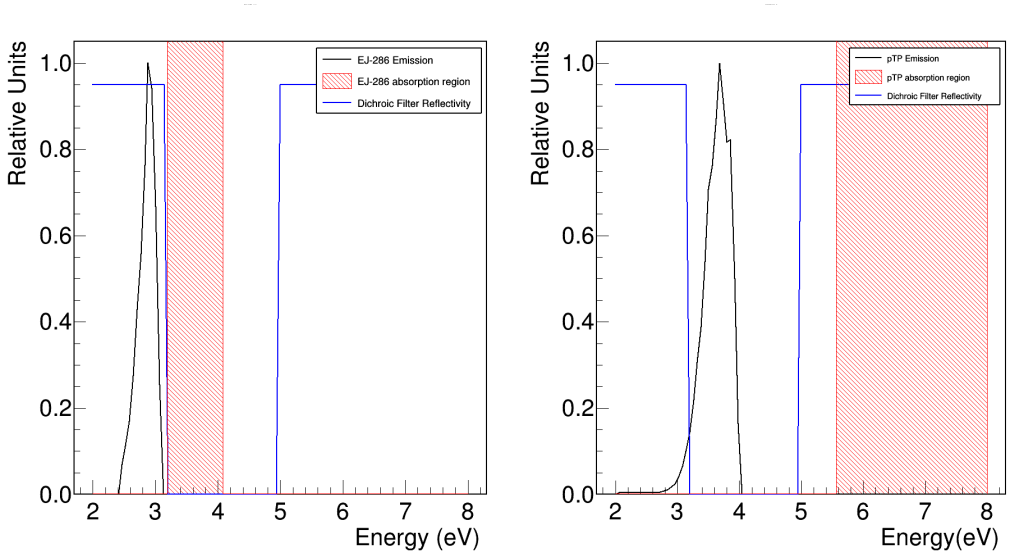


FIGURE 5.3: On the right it is possible to observe a plot of the pTP absorption region, in red; the pTP emission, in black; and the Dichroic filter reflectance, in blue. On the left it is possible to observe a graph of the EJ-286 absorption region, in red; the EJ-286 emission, in black; and the Dichroic filter reflectance, in blue.

For every implemented process, a confirmation test was performed to ensure it is executing as intended. First, the reflectivity of the materials were tested. It was performed by shining photons on it and checking how many of them are reflected. For the wavelength shifters, the emission spectrum and the conversion

efficiency were tested. It was performed irradiating the wls material with photons and acquiring all the emitted photons. The dichroic filter was also tested in the same manner. Several photons were produced and directed towards the filter, for different wavelengths. The transmitted photons were counted and checked with the implemented behaviour.

### 5.1.3 Acquisition

Finally, after the implementation an acquisition method was designed. This was implemented with the intent of retrieving all the information of the detected photon, e.g., detection position, time of detection. The data was acquired and managed using the *Geant4 G4AnalysisManager* class and it was stored in a *ROOT Ttree* file, where it can be easily accessed through the *ROOT toolkit* interface. To distinguish between photons trapped by the bar mechanism and by the ARAPUCA mechanism, several flags were implemented. The position of the detected photon is an important information, this allows the understanding of how the device is operating for the different technologies. It is possible to observe the density of detection on the surface of the SiPMs and understand how the insertion of a Light Guide Bar alters the functioning of the device. This is pictured in figure 5.4, where the average density of detection on the surface of a SiPM for an X-ARAPUCA is shown.

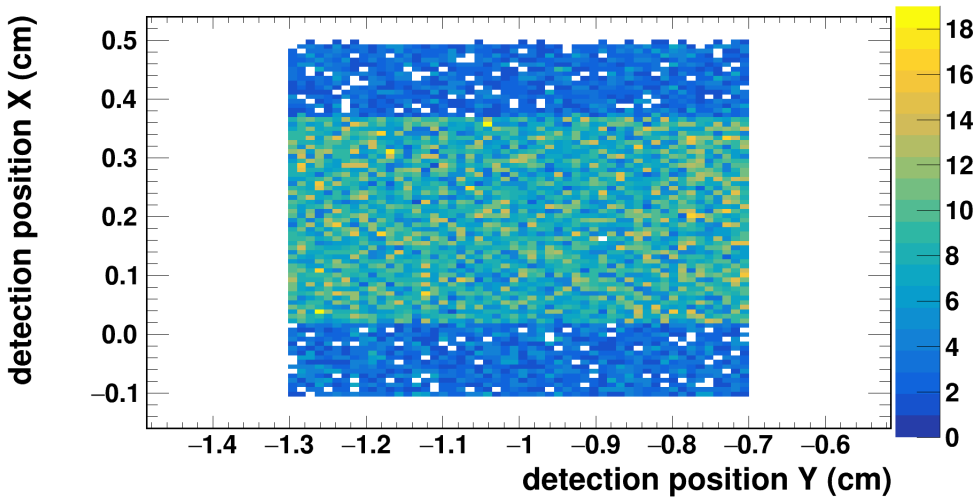


FIGURE 5.4: Histogram of the detection position in the surface of a SiPM for an X-ARAPUCA. It is possible to observe the increase in detection density where the bar is placed.

The information of the time of flight of the photons inside the detector is also important, as this has a direct influence in the device time response. It is possible to see, in figure 5.5, a waveform obtained from the simulation.

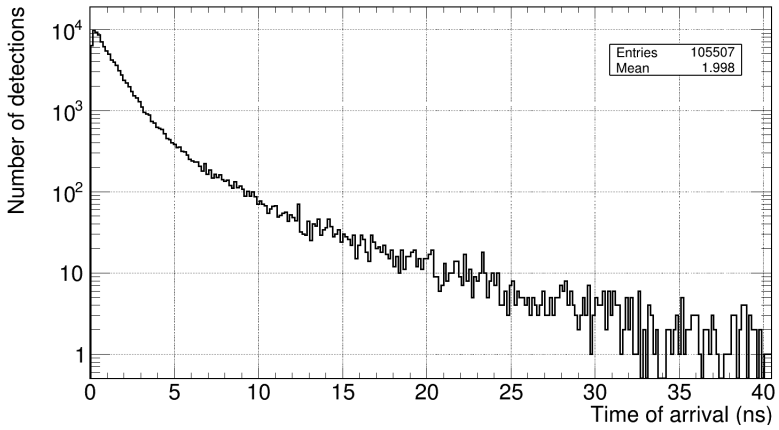


FIGURE 5.5: Histogram of the detected photons arrival time for an X-ARAPUCA

The acquisition method was subject to a series of confirmation tests, where

all sections were probed. This was done by generating photons with a known position, time stamp and direction in several sections of the device and checking the results from the acquisition pipeline.

## 5.2 Monte Carlo Results

The main objective of this chapter was to investigate how the efficiency of the X-ARAPUCA supercell module varies with the alteration of its key parameters. Also, it was intended to understand how its efficiency compares with the ARAPUCA device. The first step was to test how the efficiency of the two technologies would compare. The ARAPUCA and the X-ARAPUCA were simulated with the dimensions of a supercell for several number of SiPMs. The results are shown in figure 5.6.

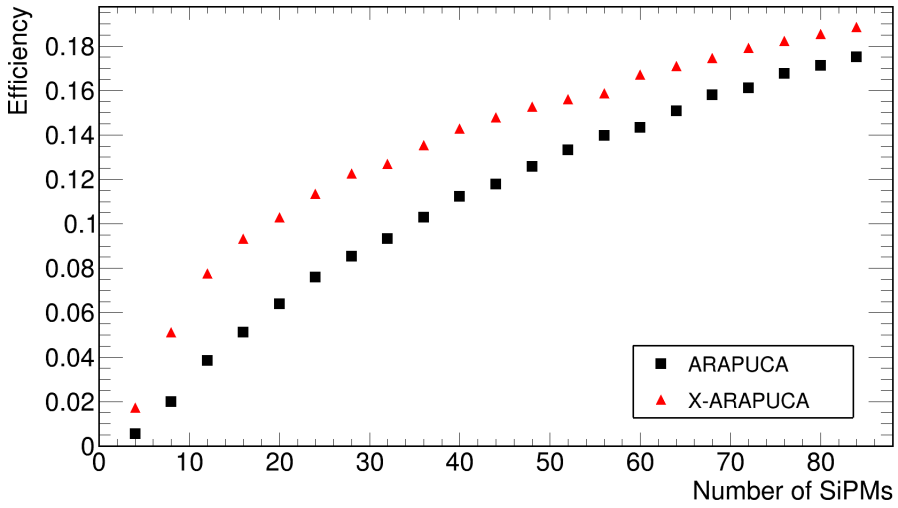


FIGURE 5.6: Efficiency comparison between the ARAPUCA and X-ARAPUCA for different number of SiPMs, calculated by the Monte Carlo simulation.

It is possible to observe that for this geometry, the X-ARAPUCA is always more efficient than the ARAPUCA device. The efficiency difference is substantial

in the interest region, around 24 SiPMs, where the X-ARAPUCA presented an efficiency of 11.3% and the ARAPUCA 7.6%.

One factor to consider is the detection mode difference, where it was observed that for a run of the X-ARAPUCA with a total efficiency of 12.5%, the Bar contributes for 7.8%, the direct detection contributes for 2.0% and the ARAPUCA method contributes for 2.8%. This results in a increase of detected photons in the region of the bar, as seen in figure 5.4.

With the higher efficiency of the X-ARAPUCA, the next tests were done to investigate how this efficiency would vary with several parameters. The first one tested was the bar thickness, pictured in figure 5.7.

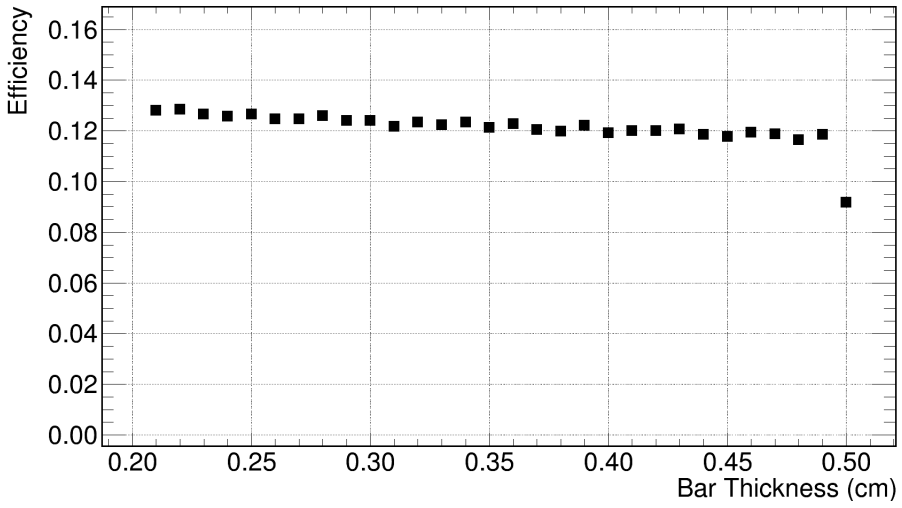


FIGURE 5.7: A graph of the X-ARAPUCA efficiency versus the bar thickness, obtained through the Monte Carlo Simulation

It is possible to see that the efficiency remains constant until the internal bar fills the X-ARAPUCA, at 0.5 *cm* thickness. In this case, the device operates like an ARAPUCA and the efficiency drops significantly.

Another test made was the investigation of the effect caused by changing the filter dichroic filter by a common fused silica plate. The results are shown in

figure 5.8.

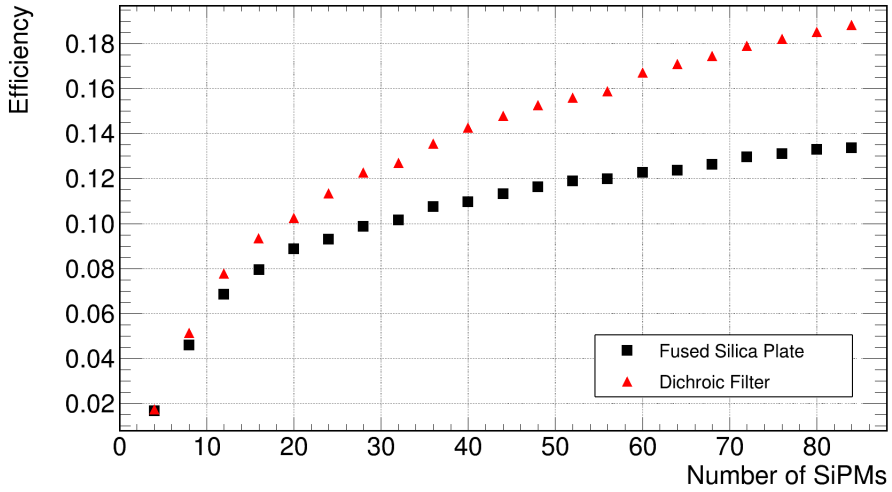


FIGURE 5.8: A comparison between the efficiency of the X-ARAPUCA equipped with a dichroic filter shown in figure 5.3 and a common fused silica plate versus the number SiPMs.

It was noticed that the X-ARAPUCA equipped with the Dichroic filter performs always better than the fused silica equipped one, with an efficiency drop comparable to the totally filled X-ARAPUCA from the figure 5.7.

Other test made was to understand how the separation between the bar and the SiPMs would affect its efficiency. For this, a simulation was performed for several separations from 0 *mm* up to 5 *mm* with a 0.1 *mm* step. The results are shown in figure 5.9.

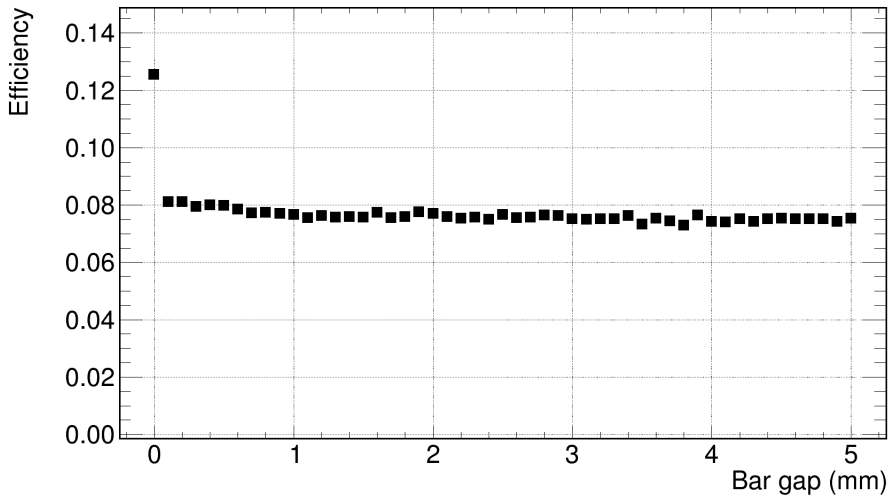


FIGURE 5.9: A graph of the X-ARAPUCA efficiency versus the gap between the bar and the SiPMs

It is possible to observe that the separation between the bar and the SiPMs affect the efficiency of the device considerably for the small separations tested. This is a result of the two surfaces not been optically coupled.

In conclusion, it was shown that for the supercell geometry the X-ARAPUCA is always more efficient that the ARAPUCA. It was also shown that the device efficiency increases with the number of SiPMs with two defined rates. The bar is shown to work best when optically coupled with the SiPMs. Its thickness does not greatly alters the efficiency of device, until it fills the whole cavity.

## 5.3 Lab Leptons tests

An experimental test of a prototype of the X-ARAPUCA device was performed in the *Laboratório de Léptons* at UNICAMP. A new simulation code was developed to investigate the efficiency of this prototype and to compare it with the experimental value. The code used was the same that was used in the previous discussion,

with an alteration on the geometry, which was changed to match the tested device. The simulated geometry is shown in figure 5.10.

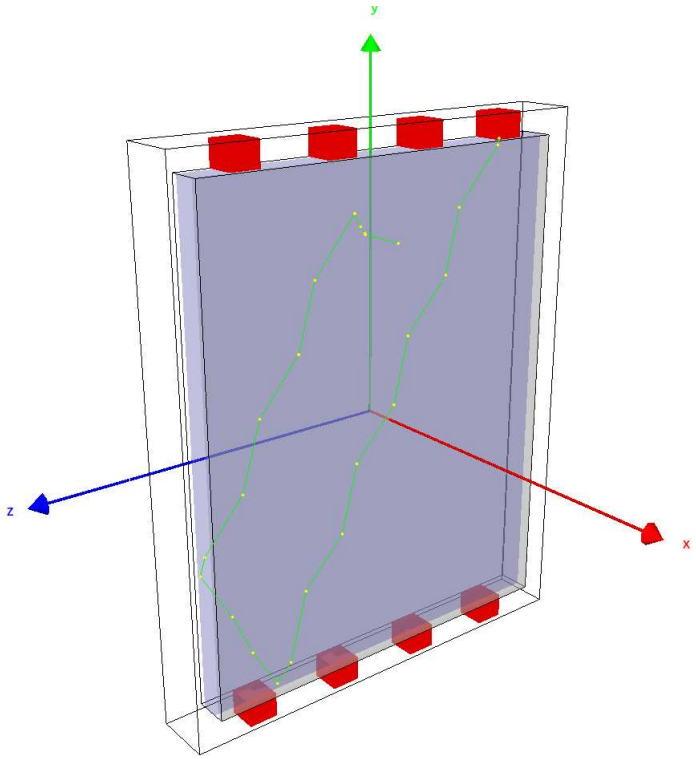


FIGURE 5.10: A picture of the simulation of one event on the X-ARAPUCA device. The internal dimensions of the device are $0.6\ cm \times 10\ cm \times 8\ cm$. The photon trajectory is seen in green and a yellow dot is placed at every step.

The geometry was constructed using the same procedure as the supercell geometry, and the parameters were kept the same. Finally, the SiPMs quantum efficiency was implemented so the simulation results could be compared with the experimental results. All the confirmation tests discussed before were done to this new code, to ensure it worked as intended. The obtained efficiency for a million events was found to be 4.2%. The reported value for the tests was $3.3\% \pm 0.2\%$. The value obtained from the simulation is higher than the one found in the experiments, which suggest that the efficiency of the X-ARAPUCA can be further improved.

# Chapter 6

# General Conclusion

In this work, several characteristics of the wavelength shifters were explored.

The first aspect approached was the hypothesis of ionization in these compounds. Using a pulsed and precise VUV light source, it was shown that this effect is present for every excitation energy tested. In particular, the tested range included 9.8 $eV$ photons, which is the central energy in Liquid Argon scintillation light. The results obtained from this analysis are close to those found in the literature, where the mean value found was $177.4 \pm 41.9$ $ns$ for the delayed light component of TPB. The following step in this analysis was to measure how the relative efficiency of these compounds would perform when exposed to VUV light, in order to understand how the ionization effect would affect the efficiency. Several samples were tested for a wide excitation range, from 6 $eV$ up to 10 $eV$. This was done as a first step in the understanding of the ionization effects on the total efficiency of this compounds. Nevertheless, using this analysis, it was possible to obtain a precise measurement of TPB efficiency versus film thickness when exposed to Liquid argon scintillation light. The results obtained are relevant, where it was possible to compare it with the literature and observe that the data not only agree with the previous measurements but also extends the measured range with greater precision.

The efficiency of the Wavelength Shifters for UV-Vis excitation light was also

measured, in order to study the best performing compound to use in combination with pTP in the ARAPUCA device. Thanks to a hint found in the measurements performed at LNLS, several measurements where performed comparing the BisMSB and TPB efficiency when illuminated by pTP light. It was found that the best performing wavelength shifter is 450 $\mu g/cm^2$ BisMSB. It is approximately 5% more efficient than TPB in any tested thickness, when excited with pTP light. This is an important result for the ARAPUCA, even though the small difference in efficiency, considering that the BisMSB cost is three times smaller than the TPB.

Finally, a Monte Carlo simulation of the ARAPUCA and the X-ARAPUCA device was constructed. It was based in the design of the standard DUNE Supercell Module, considering its dimensions and materials. This was done to understand how the efficiency of this devices varies with its construction parameters. It was shown that for the supercell geometry the X-ARAPUCA is always more efficient that the ARAPUCA. It was also shown that the device efficiency increases with the number of SiPMs with two defined rates. The bar is shown to work best when optically coupled with the SiPMs, and that its thickness does not greatly alters the efficiency of the device until it fills the whole cavity.

# Bibliography


1. Bilenky, S. Neutrino oscillations: From a historical perspective to the present status. *Nuclear Physics B* **908.** Neutrino Oscillations: Celebrating the Nobel Prize in Physics 2015, 2–13. ISSN: 0550-3213 (2016).
2. Tanabashi, M. *et al.* Review of Particle Physics. *Phys. Rev. D* **98,** 030001 (3 Aug. 2018).
3. Acciarri, R. *et al.* Long-Baseline Neutrino Facility (LBNF) and Deep Underground Neutrino Experiment (DUNE). arXiv: 1601.05471 [physics.ins-det] (2016).
4. Langacker, P. Grand Unified Theories and Proton Decay. *Phys. Rept.* **72,** 185 (1981).
5. Abi, B. *et al.* The DUNE Far Detector Interim Design Report Volume 1: Physics, Technology and Strategies. arXiv: 1807.10334 [physics.ins-det] (2018).
6. Acciarri, R. *et al.* Long-Baseline Neutrino Facility (LBNF) and Deep Underground Neutrino Experiment (DUNE). arXiv: 1512.06148 [physics.ins-det] (2015).
7. Acciarri, R. *et al.* Design and construction of the MicroBooNE detector. *Journal of Instrumentation* **12,** P02017–P02017 (Feb. 2017).
8. Abi, B. *et al.* The DUNE Far Detector Interim Design Report, Volume 2: Single-Phase Module. arXiv: 1807.10327 [physics.ins-det] (2018).
9. Whittington, D. Photon Detection System Designs for the Deep Underground Neutrino Experiment. *JINST* **11,** C05019 (2016).

10. Howard, B. *et al.* A Novel Use of Light Guides and Wavelength Shifting Plates for the Detection of Scintillation Photons in Large Liquid Argon Detectors. *Nucl. Instrum. Meth.* **A907,** 9–21 (2018).

11. Machado, A. & Segreto, E. ARAPUCA a new device for liquid argon scintillation light detection. *Journal of Instrumentation* **11,** C02004–C02004 (Feb. 2016).

12. Segreto, E. *et al.* Liquid argon test of the ARAPUCA device. *Journal of Instrumentation* **13,** P08021–P08021 (2018).

13. Machado, A. *et al.* The X-ARAPUCA: an improvement of the ARAPUCA device. *Journal of Instrumentation* **13,** C04026–C04026. ISSN: 1748-0221 (2018).

14. Miyajima, M. *et al.* Average energy expended per ion pair in liquid argon. *Phys. Rev. A* **9,** 1438–1443 (3 1974).

15. Martin, M. Exciton Self-Trapping in Rare-Gas Crystals. *The Journal of Chemical Physics* **54,** 3289–3299 (1971).

16. Druger, S. D. & Knox, R. S. Theory of Trapped-Hole Centers in Rare-Gas Solids. *The Journal of Chemical Physics* **50,** 3143–3153 (1969).

17. Xu, J. *Measurement of 39Ar in Underground Argon for Dark Matter Experiments* 2013.

18. Acciarri, R *et al.* The WArP experiment. *Journal of Physics: Conference Series* **203,** 012006 (2010).

19. Agnes, P. *et al.* First Results from the DarkSide-50 Dark Matter Experiment at Laboratori Nazionali del Gran Sasso. *Phys. Lett.* **B743,** 456–466 (2015).

20. Acciarri, R. *Measurement of the scintillation time spectra and Pulse Shape Discrimination of low-energy electron and nuclear recoils in liquid Argon with the WArP 2.3 lt detector* PhD thesis (UNIVERSITA DEGLI STUDI DE L'AQUILA).

21. Lippincott, W. H. *et al.* Scintillation time dependence and pulse shape discrimination in liquid argon. *Phys. Rev. C* **78,** 035801 (3 2008).

22. Jones, B. *INTRODUCTION TO SCINTILLATION LIGHT IN LIQUID ARGON* 2014.

23. Segreto, E. Evidence of delayed light emission of TetraPhenyl Butadiene excited by liquid Argon scintillation light. *Phys. Rev.* **C91,** 035503 (2015).

24. Gehman, V. *et al.* Fluorescence efficiency and visible re-emission spectrum of tetraphenyl butadiene films at extreme ultraviolet wavelengths. *Nuclear Instruments and Methods in Physics Research Section A: Accelerators, Spectrometers, Detectors and Associated Equipment* **654,** 116–121. ISSN: 0168-9002 (2011).

25. Stockton, M., Keto, J. W. & Fitzsimmons, W. A. Ultraviolet Emission Spectrum of Electron-Bombarded Superfluid Helium. *pra* **5,** 372–380 (Jan. 1972).

26. Packard, R. E., Reif, F. & Surko, C. M. Ultraviolet Emission Spectra of Electron-Excited Solid and Liquid Neon. *Phys. Rev. Lett.* **25,** 1435–1439 (20 Nov. 1970).

27. Saito, K., Tawara, H., Sanami, T., Shibamura, E. & Sasaki, S. Absolute number of scintillation photons emitted by alpha particles in rare gases. *IEEE Transactions on Nuclear Science* **49,** 1674–1680. ISSN: 0018-9499 (Aug. 2002).

28. *Photomultiplier Tubes: Basics and Applications* Third Edition. www.hamamatsu.com/resources/pdf/etd/PMT_handbook_v3aE.pdf (Hamamatsu Photonics).

29. Laustriat, G. The luminescence decay of organic scintilator. *Molecular Crystal 4* **62,** 127 (Jan. 1968).

30. Filho, R. C., Lago, A., Homem, M., Pilling, S. & de Brito, A. N. Delivering high-purity vacuum ultraviolet photons at the Brazilian toroidal grating monochromator (TGM) beamline. *Journal of Electron Spectroscopy and Related Phenomena* **156-158.** Electronic Spectroscopy and Structure: ICESS-10, 168–171. ISSN: 0368-2048 (2007).

31. www.lnls.cnpem.br/linhas-de-luz/tgm-en/.

32. Herb, G. K. & Van Sciver, W. J. Measurement of the Decay Time of Sodium Salicylate. *Review of Scientific Instruments* **36,** 1650–1652. ISSN: 0034-6748 (Nov. 1965).

33. Francini, R *et al.* VUV-Vis optical characterization of Tetraphenyl-butadiene films on glass and specular reflector substrates from room to liquid Argon temperature. *Journal of Instrumentation* **8,** P09006–P09006 (2013).

34. www.sigmaaldrich.com/catalog/product/aldrich/185213.

35. www.sigmaaldrich.com/catalog/product/sigma/15090.

36. Agostinelli, S. *et al.* Geant4—a simulation toolkit. *Nuclear Instruments and Methods in Physics Research Section A: Accelerators, Spectrometers, Detectors and Associated Equipment* **506,** 250–303. ISSN: 0168-9002 (2003).

37. multimedia . 3m . com / mws / media / 3747300 / vikuiti - tm - esr - sales - literature.pdf.

# Appendix A

# Sample Production

The samples used in the measurements must be produced following a process similar to that used in most scientific applications. The quality of the samples must also meet the standards used in the community.

The most used method to deposit WLSs is the Vacuum Evaporation Technique. It consists in heating the compounds under vacuum, which causes the material to evaporate. The vacuum allows the evaporated molecules to directly travel to the substrate, where it condenses. This technique, combined with a proper procedure, allows the manufacturing of precise and consistent thin films of many different materials.

The production of every sample used in the measurements discussed in this work was performed *in-lab*, using the vacuum evaporation technique. To achieve the quality standards, a procedure was designed and a dedicated machine was build. The substrate used in the evaporation was selected carefully to match the commonly used, and the samples' size were established for the experimental setup they were designated. A picture of the evaporator used is shown in figure A.1.

FIGURE A.1: A picture of the evaporator used. It is equipped with two evaporating crucibles and a rotatable substrate.

Following all the established procedures, it was possible to produce samples with grate uniformity and a precise control in its surface density. In figure A.2

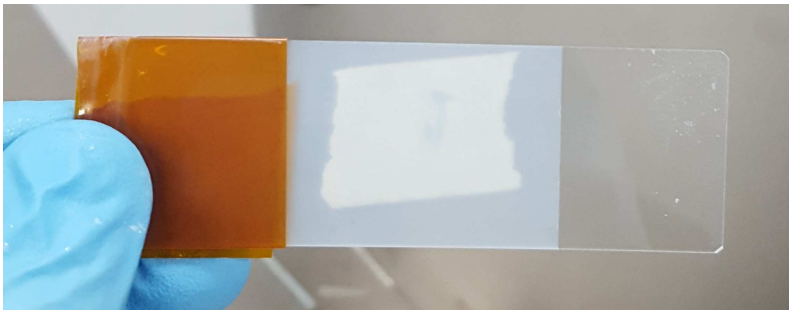

FIGURE A.2: A picture of a test TPB sample produced in the evaporator. It is possible to observe the uniformity of the sample.

A quality control procedure was developed to ensure the quality of every

batch of samples evaporated. For every evaporation, several samples were randomly selected to be subjected to three main tests. after the tests, this samples were archived and not used in the experiments.

The first test was made to ensure that the intended film thickness was achieved. For this, a *Dektak 150* Surface Profiler was used. In figure A.3 it is possible to observe a measurement of a TPB sample performed with this equipment.

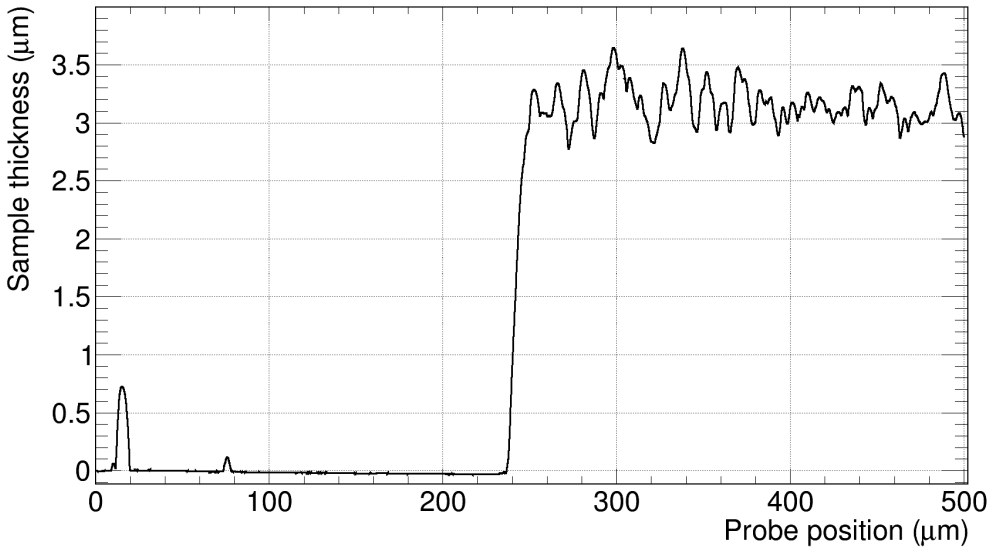


FIGURE A.3: A graph of the sample thickness obtained using the *Dektak 150* Surface Profiler.

To ensure that the measured thickness corresponds to the actual thickness, each sample was measured 5 times from different sides.

The surface uniformity of the samples was also measured. A *Nanosurf EasyScan2 FlexAFM* Atomic Force Microscope was used to study its surface. In figure A.4 it is possible to observe the surface uniformity of one sample produced.

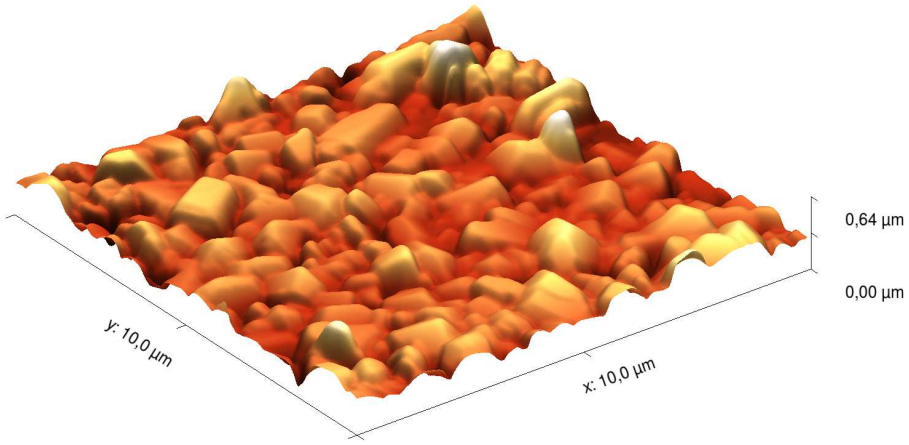


FIGURE A.4: The surface of a TPB samples. Image obtained using an Atomic Force Microscope. It is possible to observe the uniformity of the surface.

Finally, the emission spectrum of each sample was measured. This was done to ensure purity of the compounds, since any cross contamination between wavelength shifters would appear in the data. For this measurements, a *Ocean Optics QE* 65000 spectrometer was used.

# Appendix B

# Aspects of time resolved measurements

One important factor to consider while making time resolved measurements is the detector's *Impulse Response Function* (IRF). The IRF is defined as the system's response to a $\delta$ excitation. An example can be seen in figure B.1.

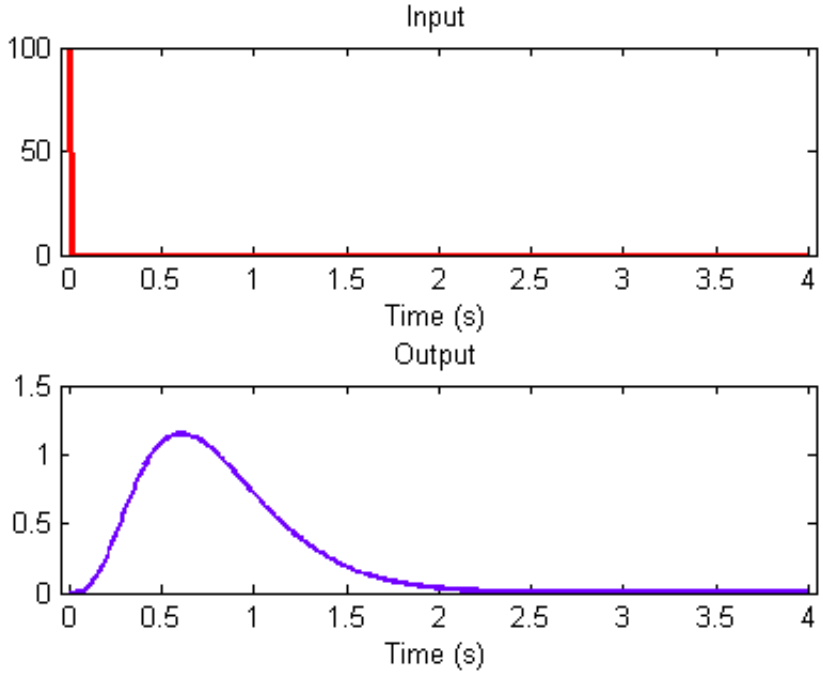


FIGURE B.1: An example of an IRF, where a system produces its own IRF signal when excited with a $\delta(t)$

To understand the effect of the IRF when measuring an arbitrary signal is important to define some concepts. Lets define $\mathscr{O}$ as the operator which acts over any signal and produces the system response. Let $x(t)$ be any arbitrary signal, and $y(t)$ the system's response to this signal, $\mathscr{O}[x(t)]$. Now, it is important to observe that the IRF is defined by $h(t) = \mathscr{O}[\delta(t)]$ and that any signal can be decomposed into $\delta$ functions, as seen in equation B.1.

$$x(t) = \int_{-\infty}^{\infty} x(\tau)\delta(t-\tau)d\tau \tag{B.1}$$

It is possible to apply the $\mathscr{O}$ operator in both sides of equation B.1. It can be noted that $x(\tau)$ and $d\tau$ are constants to the $\mathscr{O}$ operator and, by linearity, they can exit it. This results in equation B.2.

$$y(t) = \int_{-\infty}^{\infty} x(\tau)\mathscr{O}[\delta(t-\tau)]\,d\tau = \int_{-\infty}^{\infty} x(\tau)h(t-\tau)d\tau \tag{B.2}$$

Now, it is interesting to note that the last integral in the equation B.2 is precisely the *Fourier Convolution* of the arbitrary signal with the system's IRF. This can be written in a compact notation, $y(t) = x(t) * h(t)$.

Thus, we conclude that any time resolved measurements will produce a signal which is the *Fourier Convolution* of the real signal with the detectors' IRF. Furthermore, to properly analyze any measurement it is important to remove the input signal from the convoluted response. This process is called *Deconvolution*, and it is described in equation B.3.

$$x(t) = \mathscr{F}^{-1}\left[\frac{y(\omega)}{h(\omega)}\right](t), \tag{B.3}$$

where $x(t)$ is the input signal, $y(\omega)$ is the measured signal in the *Fourier space*, $h(\omega)$ is the detector's IRF in the *Fourier space* and $\mathscr{F}^{-1}$ is the *Inverse Fourier Transform*.

The deconvolution process require as inputs the measured signal and the detector's IRF. In consequence, to retrieve the real signal it is mandatory to measure the detector's IRF.